

| | | | | | |
|---|-------------------|--------------------------------|---|--|---|
| REPORT DOCUMENTATION PAGE | | | Form Approved OMB NO. 0704-0188 | | |
| <p>The public reporting burden for this collection of information is estimated to average 1 hour per response, including the time for reviewing instructions, searching existing data sources, gathering and maintaining the data needed, and completing and reviewing the collection of information. Send comments regarding this burden estimate or any other aspect of this collection of information, including suggestions for reducing this burden, to Washington Headquarters Services, Directorate for Information Operations and Reports, 1215 Jefferson Davis Highway, Suite 1204, Arlington VA, 22202-4302. Respondents should be aware that notwithstanding any other provision of law, no person shall be subject to any penalty for failing to comply with a collection of information if it does not display a currently valid OMB control number.</p> <p>PLEASE DO NOT RETURN YOUR FORM TO THE ABOVE ADDRESS.</p> | | | | | |
| 1. REPORT DATE (DD-MM-YYYY) 28-11-2012 | | 2. REPORT TYPE Final Report | | 3. DATES COVERED (From - To) 1-Sep-2009 - 31-Aug-2012 | |
| 4. TITLE AND SUBTITLE Final Progress Report | | | 5a. CONTRACT NUMBER W911NF-09-1-0488 | | |
| | | | 5b. GRANT NUMBER | | |
| | | | 5c. PROGRAM ELEMENT NUMBER 611102 | | |
| 6. AUTHORS Dirk Gillespie | | | 5d. PROJECT NUMBER | | |
| | | | 5e. TASK NUMBER | | |
| | | | 5f. WORK UNIT NUMBER | | |
| 7. PERFORMING ORGANIZATION NAMES AND ADDRESSES Rush University Rush University Medical Center 1653 W Congress Parkway Chicago, IL 60612 -0000 | | | 8. PERFORMING ORGANIZATION REPORT NUMBER | | |
| 9. SPONSORING/MONITORING AGENCY NAME(S) AND ADDRESS(ES) U.S. Army Research Office P.O. Box 12211 Research Triangle Park, NC 27709-2211 | | | 10. SPONSOR/MONITOR'S ACRONYM(S) ARO | | |
| | | | 11. SPONSOR/MONITOR'S REPORT NUMBER(S) 56381-MS.16 | | |
| 12. DISTRIBUTION AVAILABILITY STATEMENT Approved for Public Release; Distribution Unlimited | | | | | |
| 13. SUPPLEMENTARY NOTES The views, opinions and/or findings contained in this report are those of the author(s) and should not be construed as an official Department of the Army position, policy or decision, unless so designated by other documentation. | | | | | |
| 14. ABSTRACT This is a final progress report, detailing the scientific methods used to derive a classical density functional theory for dielectric interfaces and their fast numerical implementation. | | | | | |
| 15. SUBJECT TERMS progress report | | | | | |
| 16. SECURITY CLASSIFICATION OF: | | | 17. LIMITATION OF ABSTRACT UU | 15. NUMBER OF PAGES | 19a. NAME OF RESPONSIBLE PERSON Dirk Gillespie |
| a. REPORT UU | b. ABSTRACT UU | c. THIS PAGE UU | | | 19b. TELEPHONE NUMBER 312-942-3089 |

Report Title

Final Progress Report

ABSTRACT

This is a final progress report, detailing the scientific methods used to derive a classical density functional theory for dielectric interfaces and their fast numerical implementation.

Enter List of papers submitted or published that acknowledge ARO support from the start of the project to the date of this printing. List the papers, including journal references, in the following categories:

(a) Papers published in peer-reviewed journals (N/A for none)

| <u>Received</u> | <u>Paper</u> |
|-----------------|--------------|
|-----------------|--------------|

TOTAL:

Number of Papers published in peer-reviewed journals:

(b) Papers published in non-peer-reviewed journals (N/A for none)

| <u>Received</u> | <u>Paper</u> |
|-----------------|--------------|
|-----------------|--------------|

TOTAL:

Number of Papers published in non peer-reviewed journals:

(c) Presentations

1. oral presentation at annual meeting of the American Physical Society 2010, "Classical density functional theory of fluids □ as a multi-scale modeling tool for charged fluids: Electrical double layers, Biological ion channels, Dielectric interfaces"
2. seminar at University of Pannonia, 2010, "Recent developments in □ density functional theory of fluids"
3. poster presentation at Liblice Meeting on Statistical Mechanics, 2010, "A density functional theory of ions at a dielectric interface"
4. oral presentation at annual meeting of American Institute of Chemical Engineers (AIChE), 2011, "Efficiently accounting for □ ion correlations in nanofluidic devices □ using Density Functional Theory"
5. oral presentation at International Congress of Industrial and Applied Mathematics, 2011, "Electrodiffusion of Hard-Sphere Ions with Density Functional Theory of Fluids"
6. poster presentation at Liquid Matter conference, 2011, "Efficiently accounting for □ ion correlations in nanofluidic devices □ using Density Functional Theory"
7. seminar at Mathematical Biosciences Institute of The Ohio State University, 2011, "Modeling ion size effects with □ density functional theory of fluids"
8. seminar at Dept. of Material Sciences of University of Washington, 2011, "Designing Devices Based on □ Ion-Ion Correlations in □ Biology, Nanofluidics, and Beyond"
9. oral presentation at ICREA Symposium 2012 on Nanofluidics, Colloids, and Membranes, 2012, "Exploiting ion-ion correlations in nanofluidic channels"
10. oral presentation at Society for Industrial and Applied Mathematics (SIAM) Life Sciences meeting, 2012, "Multiscale modeling of □ ion correlations in proteins with □ density functional theory of liquids"
11. seminar at Institute for Nanotechnology of the University of Twente, 2012, "Designing Devices Based on □ Ion-Ion Correlations in □ Biology, Nanofluidics, and Beyond"
12. seminar in Dept. of Mechanical Engineering of Stanford University, 2012, "Designing Devices Based on □ Ion-Ion Correlations in □ Biology, Nanofluidics, and Beyond"

Number of Presentations: 12.00

Non Peer-Reviewed Conference Proceeding publications (other than abstracts):

| <u>Received</u> | <u>Paper</u> |
|-----------------|--------------|
|-----------------|--------------|

TOTAL:

Number of Non Peer-Reviewed Conference Proceeding publications (other than abstracts):

Peer-Reviewed Conference Proceeding publications (other than abstracts):

Received Paper

TOTAL:

Number of Peer-Reviewed Conference Proceeding publications (other than abstracts):

(d) Manuscripts

Received Paper

| | | |
|------------|------|---|
| 01/07/2011 | 4.00 | Dirk Gillespie. Preprint of Towards making the mean spherical approximation (MSA) of primitive model electrolytes analytic: An analytic approximation of the MSA screening parameter, Journal of Chemical Physics (01 2011) |
| 08/27/2010 | 3.00 | Felipe A. Cruz, Matthew G. Knepley, L. A. Barba. Manuscript: PetFMM--A dynamically load-balancing parallel fast multipole library, International Journal for Numerical Methods in Engineering (03 2010) |
| 10/13/2009 | 1.00 | Matthew G. Knepley, Dmitry A. Karpeev, Seth Davidovits, Robert S. Eisenberg, Dirk Gillespie. An Efficient Algorithm for Classical Density Functional Theory in Three Dimensions: Ionic Solutions, Journal of Chemical Physics (10 2009) |

TOTAL: 3

Number of Manuscripts:

Books

Received Paper

TOTAL:

Patents Submitted

Patents Awarded

Awards

PI Gillespie received tenure and a promotion to Associate Professor

Graduate Students

| <u>NAME</u> | <u>PERCENT SUPPORTED</u> |
|-------------|--------------------------|
|-------------|--------------------------|

FTE Equivalent:

Total Number:

Names of Post Doctorates

| <u>NAME</u> | <u>PERCENT SUPPORTED</u> |
|-------------|--------------------------|
|-------------|--------------------------|

FTE Equivalent:

Total Number:

Names of Faculty Supported

| <u>NAME</u> | <u>PERCENT SUPPORTED</u> | National Academy Member |
|-------------|--------------------------|-------------------------|
|-------------|--------------------------|-------------------------|

Matthew G. Knepley

0.10

FTE Equivalent:

0.10

Total Number:

1

Names of Under Graduate students supported

| <u>NAME</u> | <u>PERCENT SUPPORTED</u> | Discipline |
|-------------|--------------------------|------------|
|-------------|--------------------------|------------|

Jordan Hoffmann

0.00

biophysics

FTE Equivalent:

0.00

Total Number:

1

Student Metrics

This section only applies to graduating undergraduates supported by this agreement in this reporting period

The number of undergraduates funded by this agreement who graduated during this period: 1.00

The number of undergraduates funded by this agreement who graduated during this period with a degree in science, mathematics, engineering, or technology fields:..... 1.00

The number of undergraduates funded by your agreement who graduated during this period and will continue to pursue a graduate or Ph.D. degree in science, mathematics, engineering, or technology fields:..... 1.00

Number of graduating undergraduates who achieved a 3.5 GPA to 4.0 (4.0 max scale):..... 0.00

Number of graduating undergraduates funded by a DoD funded Center of Excellence grant for Education, Research and Engineering:..... 0.00

The number of undergraduates funded by your agreement who graduated during this period and intend to work for the Department of Defense 0.00

The number of undergraduates funded by your agreement who graduated during this period and will receive scholarships or fellowships for further studies in science, mathematics, engineering or technology fields: 0.00

Names of Personnel receiving masters degrees

| <u>NAME</u> |
|-------------|
|-------------|

Total Number:

Names of personnel receiving PhDs

| |
|-------------|
| <u>NAME</u> |
|-------------|

| |
|---------------|
| Total Number: |
|---------------|

Names of other research staff

| |
|-------------|
| <u>NAME</u> |
|-------------|

| |
|--------------------------|
| <u>PERCENT SUPPORTED</u> |
|--------------------------|

| |
|-----------------|
| FTE Equivalent: |
|-----------------|

| |
|---------------|
| Total Number: |
|---------------|

Sub Contractors (DD882)

Inventions (DD882)

Scientific Progress

See Attachment

Technology Transfer

Final Progress Report for W911NF-09-1-0488

PI: Dirk Gillespie

November 23, 2012

Contents

| | | |
|----------|--|-----------|
| 1 | Summary of Progress | 1 |
| 2 | Technical Details of Dielectric DFT Implementation | 2 |
| 2.1 | Perturbation theory | 3 |
| 2.2 | Single planar dielectric interface | 6 |
| 2.3 | Ion TCF | 7 |
| 2.3.1 | Scaling of ion TCF | 8 |
| 2.4 | Dielectric TCF | 10 |
| 2.4.1 | Scaling the dielectric TCF | 12 |
| 2.5 | Wall component | 14 |
| 2.6 | Toward an efficient numerical implementation | 15 |
| 3 | Technical Details of FMM Implementation (written by Dr. Matt Knepley) | 15 |
| 3.1 | FMM Overview | 15 |
| 3.2 | Parallel Strategy | 16 |
| 3.3 | Electrostatics | 17 |
| 4 | Implementation of the FMM method (written by Dr. Matt Knepley) | 17 |
| 4.1 | DFT Development | 18 |
| 4.2 | Electrostatics | 18 |
| 4.2.1 | Using FMM | 19 |
| 4.2.2 | BIBEE Approximation | 20 |
| 5 | Local Equilibrium Grand Canonical Monte Carlo | 20 |
| 6 | Connecting with experiments in nanofluidic devices | 22 |

1 Summary of Progress

The overall (three-year) goal of the proposed work is to develop a classical density functional theory (DFT) of ions and charged polymers near dielectric interfaces in a three-dimensional system. Over the 3 years of the grant, we have had great success and some setbacks, as might be expected for any research project. These include:

- The biggest success was publication of the paper describing the general theory in *Journal of Physical Chemistry Letters*. This is the big theory paper to come out of this project and represents the most important goal of the proposed work (i.e., constructing the functional itself). In the year since publication, it has already been cited 3 times, indicating an impact of the work.

- Numerical implementation of an efficient algorithm to solve the dielectric DFT equations is still being implemented and work on this front will continue beyond the completion of the grant. This is the biggest setback of the project. The finding of an efficient algorithm to numerically solve the dielectric DFT equations was much more difficult than anticipated. The root of the problem is that the reaction field is not a radial interaction between ions. Because of this, fast Fourier transforms (FFTs) can no longer be used and one must be clever in making the program scale with $N \log N$ rather than N^2 where N is the number of grid points to be solved.
- On the other hand, one great numerical success was in implementing fast computational methods for the reaction in 3D. Matt Knepley at the Computational Institute of the University of Chicago, through a subcontract of this grant, has implemented a Fast Multipole Method (FMM) and published a paper on this topic.
- An exciting offshoot of the DFT work was a collaboration with Dezső Boda in Hungary that resulted in an alternative method (not using DFT at all) of ions at dielectric interfaces that we developed. The specific goal of the proposed work is to develop a DFT of ions at a dielectric interface and this has been done (as just mentioned). The broader goal of the proposed work is develop methods that any scientist can use when working with ions at a dielectric interface, especially in three dimensional geometries. We have started to develop another method with Dr. Boda, a long-time collaborator, called the Local Equilibrium Grand Canonical Monte Carlo (LE-GCMC). Because we have already developed a fast method to include dielectrics in Monte Carlo, this method will allow for computing ion currents (currently at the drift-diffusion level, but not limited to that) in complex 3D geometries that will be very challenging with DFT. The grant sponsored Dr. Boda's one month visit to the PI's institution to work on this. It is important to note that this work is *in addition* to the DFT development; LE-GCMC came out of discussions that Dr. Boda and the PI had in discussing the dielectric DFT. Moreover, Dr. Boda's visit helped greatly in moving toward an efficient algorithm to numerically solve the dielectric DFT equations.
- Another offshoot of this work is the hope of coupling the new dielectric DFT functional to experiments. This work, which will continue beyond the completion of the grant, is with experimentalists working on nanofluidic devices. This resulted in 2 papers (a third is in preparation), including one in the prestigious *Nano Letters*.

Below, a technical summary of the scientific work done over the course of the grant is given.

2 Technical Details of Dielectric DFT Implementation

In the following ions are in dielectric ϵ near a dielectric interface with dielectric constant ϵ_{wall} . The interface is assumed to be smooth and hard so that ions (assumed to be charged, hard spheres) cannot overlap any part of the wall dielectric. The goal is write down an approximate free energy functional $F^D[\{\rho_k(\mathbf{x})\}]$ to determine the ion density profiles $\rho_i(\mathbf{x})$ for all the ion species i . This is done by finding the dielectric component of the electrochemical potential, which is given by the functional derivative of F^D (i.e., $\delta F^D/\delta \rho_i(\mathbf{x})$). The total electrochemical potential (of which we only determine one component in the proposed work) is then used to find the equilibrium density profiles $\rho_i(\mathbf{x})$. These are plotted in Fig. 1.

divalent

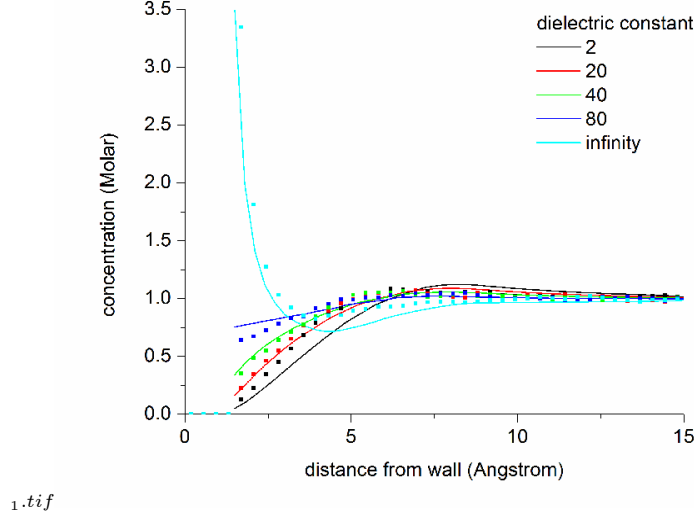


Figure 1: Comparison of the new dielectric DFT (lines) with MC simulations (symbols) for five different dielectric constants of the wall (the ions' dielectric constant is always 80). Top panel: 0.1 M monovalent ions, both with diameter 3 Å. Both cation and anion profiles are identical in this case so only one is shown. Bottom panel: 1 M divalent cation and 2 M monovalent anions, both with diameter 3 Å. The cation profile is shown.

2.1 Perturbation theory

For a general three dimension system, the interaction potential perturbation technique gives that the dielectric contribution to the free energy functional is given by

$$F^D [\{\rho_k(\mathbf{x})\}] = \frac{1}{2} \sum_{i,j} \int_0^1 \int \int \rho_{ij}^{(2)}(\mathbf{x}, \mathbf{x}'; \alpha) \psi_{ij}^D(\mathbf{x}, \mathbf{x}') d\mathbf{x} d\mathbf{x}' d\alpha \quad (1)$$

$$+ \frac{1}{2} \sum_i \int \rho_i(\mathbf{x}) \psi_{ii}^D(\mathbf{x}, \mathbf{x}) d\mathbf{x}$$

where $\rho_{ij}^{(2)}(\mathbf{x}, \mathbf{x}'; \alpha)$ is the two-body distribution function for an ion of species i at \mathbf{x} and an ion of species j at \mathbf{x}' for the interaction potential

$$\psi_{ij}(\mathbf{x}, \mathbf{x}') = \psi_{ij}^C(\mathbf{x}, \mathbf{x}') + \alpha \psi_{ij}^D(\mathbf{x}, \mathbf{x}') \quad (2)$$

with $\psi_{ij}^C(\mathbf{x}, \mathbf{x}')$ the Coulomb interaction and $\psi_{ij}^D(\mathbf{x}, \mathbf{x}')$ the dielectric reaction potential (i.e., the potential felt by an ion with valence z_j at \mathbf{x}' produced by an ion with valence z_i at \mathbf{x}). When the system has a planar dielectric interface,

$$\psi_{ij}^D(\mathbf{x}, \mathbf{x}') \propto \frac{\epsilon - \epsilon_{\text{wall}}}{\epsilon + \epsilon_{\text{wall}}}. \quad (3)$$

(This is still a very good approximation even when the dielectric interface is not a plane.) Therefore, we can make the correspondence

$$\alpha = \left| \frac{\epsilon - \epsilon_{\alpha}}{\epsilon + \epsilon_{\alpha}} \right| \quad (4)$$

where ϵ_{α} ranges between ϵ and ϵ_{wall} . (The absolute value is necessary to prevent $\alpha < 0$ when $\epsilon_{\text{wall}} > \epsilon$.)

We first describe the two-body distribution function in terms of a pair correlation function $g_{ij}(\mathbf{x}, \mathbf{x}'; \alpha)$:

$$\rho_{ij}^{(2)}(\mathbf{x}, \mathbf{x}'; \alpha) = \rho_i(\mathbf{x}; \alpha) \rho_j(\mathbf{x}'; \alpha) g_{ij}(\mathbf{x}, \mathbf{x}'; \alpha). \quad (5)$$

We know that

$$g_{ij}(\mathbf{x}, \mathbf{x}'; \alpha) = 0 \quad (|\mathbf{x} - \mathbf{x}'| < R_i + R_j) \quad (6)$$

when the ions overlap and that when $\alpha = 0$ only the ion-ion correction $h_{ij}^{\text{ion}}(\mathbf{x}, \mathbf{x}')$ and the $\alpha = 0$ ion profile near the wall contribute. Each of these factors is approximated. First, we assume that the densities ρ_k change linearly with α :

$$\rho_k(\mathbf{x}; \alpha) = \left(\rho_k(\mathbf{x}) - \rho_k^{(0)}(\mathbf{x}) \right) \alpha + \rho_k^{(0)}(\mathbf{x}) \quad (7)$$

where $\rho_k(\mathbf{x})$ is the density profile we aim to calculate ($\alpha = 1$) and $\rho_k^{(0)}(\mathbf{x})$ is the density profile of the unperturbed system in the absence of dielectric interfaces ($\alpha = 0$) for which we presume there is a good DFT available. This linear change with α has been verified in the Monte Carlo simulation results of Fig. 1.

Second, we assume that the total correlation function (TCF) is the sum of TCFs, one from an ion of species i at \mathbf{x} and one from its image charge, with a residual term from the case of no induced charge:

$$g_{ij}(\mathbf{x}, \mathbf{x}'; \alpha) - 1 \approx h_{ij}^{\text{ion}}(\mathbf{x}, \mathbf{x}') + h_{ij}^{\text{wall}}(\mathbf{x}') + h_{ij}^D(\mathbf{x}, \mathbf{x}'; \alpha). \quad (8)$$

The dielectric TCF is due to ions packing around the image charge which we assume (by Debye-Hückel) is proportional to the magnitude of the image charge and is otherwise the bulk TCF:

$$h_{ij}^D(\mathbf{x}, \mathbf{x}'; \alpha) \approx \frac{\epsilon - \epsilon_{\text{wall}}}{\epsilon + \epsilon_{\text{wall}}} h_{ij}^D(\mathbf{x}^*, \mathbf{x}') = \alpha \cdot \text{sgn} \left(\frac{\epsilon - \epsilon_{\text{wall}}}{\epsilon + \epsilon_{\text{wall}}} \right) \cdot h_{ij}^D(\mathbf{x}^*, \mathbf{x}') \quad (9)$$

where the location of the image charge is \mathbf{x}^* (which is a function of \mathbf{x}). Therefore,

$$g_{ij}(\mathbf{x}, \mathbf{x}'; \alpha) - 1 \approx \begin{cases} h_{ij}^{\text{ion}}(\mathbf{x}, \mathbf{x}') + h_{ij}^{\text{wall}}(\mathbf{x}') + \alpha \cdot \text{sgn} \left(\frac{\epsilon - \epsilon_{\text{wall}}}{\epsilon + \epsilon_{\text{wall}}} \right) \cdot h_{ij}^D(\mathbf{x}^*, \mathbf{x}') & |\mathbf{x} - \mathbf{x}'| \geq R_i + R_j \\ -1 & |\mathbf{x} - \mathbf{x}'| < R_i + R_j \end{cases} \quad (10)$$

If we chose h_{ij}^{ion} to be the bulk TCF h_{ij}^{bulk} , then the total charge from the ions around the central ion would not necessarily cancel the central charge. Therefore, h_{ij}^{ion} is defined as a rescaled bulk TCF:

$$h_{ij}^{\text{ion}}(\mathbf{x}, \mathbf{x}') = \begin{cases} \chi_i(\mathbf{x}) h_{ij}^{\text{bulk}}(|\mathbf{x} - \mathbf{x}'|) & \text{if } |\mathbf{x} - \mathbf{x}'| \geq R_{ij} \\ -1 & \text{otherwise} \end{cases} \quad (11)$$

where

$$\chi_i(\mathbf{x}) = \frac{-z_i e}{\sum_j q_{ij}(\mathbf{x})} \quad (12)$$

with

$$q_{ij}(\mathbf{x}) = z_j e \rho_j^{\text{bath}} \int_{|\mathbf{x} - \mathbf{x}'| \geq R_{ij}} h_{ij}^{\text{ion}}(|\mathbf{x} - \mathbf{x}'|) e^{-V_j^{\text{ext}}(\mathbf{x}')/kT} d\mathbf{x}'. \quad (13)$$

$q_{ij}(\mathbf{x})$ is the charge of species j around an ion of species i located at \mathbf{x} . By the overlap condition in Eq. (6), we then require that h_{ij}^{wall} and h_{ij}^D are 0 when $|\mathbf{x} - \mathbf{x}'| < R_i + R_j$.

The uncharged wall TCF h_{ij}^{wall} is nothing but the ion profile of the ions when $\alpha = 0$:

$$h_{ij}^{\text{wall}}(\mathbf{x}') = \begin{cases} \frac{\rho_j^{(0)}(\mathbf{x}')}{\rho_j^{\text{bath}}} - 1 & |\mathbf{x} - \mathbf{x}'| \geq R_i + R_j \\ 0 & |\mathbf{x} - \mathbf{x}'| < R_i + R_j. \end{cases} \quad (14)$$

With these approximations,

$$F^D [\{\rho_k(\mathbf{x})\}] - \frac{1}{2} \sum_i \int \rho_i(\mathbf{x}) \psi_{ii}^D(\mathbf{x}, \mathbf{x}) d\mathbf{x} \approx \frac{1}{2} \sum_{i,j} \int_0^1 \int \int \left[\left(\rho_i(\mathbf{x}) - \rho_i^{(0)}(\mathbf{x}) \right) \alpha + \rho_i^{(0)}(\mathbf{x}) \right] \left[\left(\rho_j(\mathbf{x}') - \rho_j^{(0)}(\mathbf{x}') \right) \alpha + \rho_j^{(0)}(\mathbf{x}') \right] \quad (15)$$

$$\begin{aligned} & \times \left(h_{ij}^{\text{ion}}(\mathbf{x}, \mathbf{x}') + h_{ij}^{\text{wall}}(\mathbf{x}') + \alpha \cdot \text{sgn} \left(\frac{\epsilon - \epsilon_{\text{wall}}}{\epsilon + \epsilon_{\text{wall}}} \right) \cdot h_{ij}^D(\mathbf{x}^*, \mathbf{x}') + 1 \right) \psi_{ij}^D(\mathbf{x}, \mathbf{x}') d\mathbf{x} d\mathbf{x}' d\alpha \\ & = \frac{1}{6} \sum_{i,j} \int \int \left(\rho_i(\mathbf{x}) - \rho_i^{(0)}(\mathbf{x}) \right) \left(\rho_j(\mathbf{x}') - \rho_j^{(0)}(\mathbf{x}') \right) \left(h_{ij}^{\text{ion}}(\mathbf{x}, \mathbf{x}') + 1 + h_{ij}^{\text{wall}}(\mathbf{x}') \right) \psi_{ij}^D(\mathbf{x}, \mathbf{x}') d\mathbf{x} d\mathbf{x}' \quad (16) \\ & + \frac{1}{4} \sum_{i,j} \int \int \left(\rho_i(\mathbf{x}) - \rho_i^{(0)}(\mathbf{x}) \right) \rho_j^{(0)}(\mathbf{x}') \left(h_{ij}^{\text{ion}}(\mathbf{x}, \mathbf{x}') + 1 + h_{ij}^{\text{wall}}(\mathbf{x}') \right) \psi_{ij}^D(\mathbf{x}, \mathbf{x}') d\mathbf{x} d\mathbf{x}' \\ & + \frac{1}{4} \sum_{i,j} \int \int \left(\rho_j(\mathbf{x}') - \rho_j^{(0)}(\mathbf{x}') \right) \rho_i^{(0)}(\mathbf{x}) \left(h_{ij}^{\text{ion}}(\mathbf{x}, \mathbf{x}') + 1 + h_{ij}^{\text{wall}}(\mathbf{x}') \right) \psi_{ij}^D(\mathbf{x}, \mathbf{x}') d\mathbf{x} d\mathbf{x}' \\ & + \frac{1}{2} \sum_{i,j} \int \int \rho_i^{(0)}(\mathbf{x}) \rho_j^{(0)}(\mathbf{x}') \left(h_{ij}^{\text{ion}}(\mathbf{x}, \mathbf{x}') + 1 + h_{ij}^{\text{wall}}(\mathbf{x}') \right) \psi_{ij}^D(\mathbf{x}, \mathbf{x}') d\mathbf{x} d\mathbf{x}' \\ & + \frac{1}{8} \text{sgn} \left(\frac{\epsilon - \epsilon_{\text{wall}}}{\epsilon + \epsilon_{\text{wall}}} \right) \sum_{i,j} \int \int \left(\rho_i(\mathbf{x}) - \rho_i^{(0)}(\mathbf{x}) \right) \left(\rho_j(\mathbf{x}') - \rho_j^{(0)}(\mathbf{x}') \right) h_{ij}^D(\mathbf{x}^*, \mathbf{x}') \psi_{ij}^D(\mathbf{x}, \mathbf{x}') d\mathbf{x} d\mathbf{x}' \\ & + \frac{1}{6} \text{sgn} \left(\frac{\epsilon - \epsilon_{\text{wall}}}{\epsilon + \epsilon_{\text{wall}}} \right) \sum_{i,j} \int \int \left(\rho_i(\mathbf{x}) - \rho_i^{(0)}(\mathbf{x}) \right) \rho_j^{(0)}(\mathbf{x}') h_{ij}^D(\mathbf{x}^*, \mathbf{x}') \psi_{ij}^D(\mathbf{x}, \mathbf{x}') d\mathbf{x} d\mathbf{x}' \\ & + \frac{1}{6} \text{sgn} \left(\frac{\epsilon - \epsilon_{\text{wall}}}{\epsilon + \epsilon_{\text{wall}}} \right) \sum_{i,j} \int \int \left(\rho_j(\mathbf{x}') - \rho_j^{(0)}(\mathbf{x}') \right) \rho_i^{(0)}(\mathbf{x}) h_{ij}^D(\mathbf{x}^*, \mathbf{x}') \psi_{ij}^D(\mathbf{x}, \mathbf{x}') d\mathbf{x} d\mathbf{x}' \\ & + \frac{1}{4} \text{sgn} \left(\frac{\epsilon - \epsilon_{\text{wall}}}{\epsilon + \epsilon_{\text{wall}}} \right) \sum_{i,j} \int \int \rho_i^{(0)}(\mathbf{x}) \rho_j^{(0)}(\mathbf{x}') h_{ij}^D(\mathbf{x}^*, \mathbf{x}') \psi_{ij}^D(\mathbf{x}, \mathbf{x}') d\mathbf{x} d\mathbf{x}' \end{aligned}$$

Then

$$\begin{aligned} \mu_i^D(\mathbf{x}) & \equiv \frac{\delta F^D}{\delta \rho_i(\mathbf{x})} \\ & \approx \frac{1}{3} \sum_j \int \left(\rho_j(\mathbf{x}') - \rho_j^{(0)}(\mathbf{x}') \right) \left(h_{ij}^{\text{ion}}(\mathbf{x}, \mathbf{x}') + 1 + h_{ij}^{\text{wall}}(\mathbf{x}') \right) \psi_{ij}^D(\mathbf{x}, \mathbf{x}') d\mathbf{x}' \quad (17) \\ & + \frac{1}{2} \sum_j \int \rho_j^{(0)}(\mathbf{x}') \left(h_{ij}^{\text{ion}}(\mathbf{x}, \mathbf{x}') + 1 + h_{ij}^{\text{wall}}(\mathbf{x}') \right) \psi_{ij}^D(\mathbf{x}, \mathbf{x}') d\mathbf{x}' \\ & + \frac{1}{4} \text{sgn} \left(\frac{\epsilon - \epsilon_{\text{wall}}}{\epsilon + \epsilon_{\text{wall}}} \right) \sum_j \int \left(\rho_j(\mathbf{x}') - \rho_j^{(0)}(\mathbf{x}') \right) h_{ij}^D(\mathbf{x}^*, \mathbf{x}') \psi_{ij}^D(\mathbf{x}, \mathbf{x}') d\mathbf{x}' \\ & + \frac{1}{3} \text{sgn} \left(\frac{\epsilon - \epsilon_{\text{wall}}}{\epsilon + \epsilon_{\text{wall}}} \right) \sum_j \int \rho_j^{(0)}(\mathbf{x}') h_{ij}^D(\mathbf{x}^*, \mathbf{x}') \psi_{ij}^D(\mathbf{x}, \mathbf{x}') d\mathbf{x}' \\ & + \frac{1}{2} \psi_{ii}^D(\mathbf{x}, \mathbf{x}). \end{aligned}$$

This can be rewritten because the terms without the correlation function are solutions to Poisson equations:

$$\mu_i^D(\mathbf{x}) \approx \sum_j \int \left(\frac{1}{3} \rho_j(\mathbf{x}') + \frac{1}{6} \rho_j^{(0)}(\mathbf{x}') \right) h_{ij}^{\text{ion}}(\mathbf{x}, \mathbf{x}') \psi_{ij}^D(\mathbf{x}, \mathbf{x}') d\mathbf{x}' \quad (18)$$

$$\begin{aligned} & + \frac{1}{3} z_i e \phi_D(\mathbf{x}) + \frac{1}{6} z_i e \phi_D^{(0)}(\mathbf{x}) \\ & + \sum_j \int \left(\frac{1}{3} \rho_j(\mathbf{x}') + \frac{1}{6} \rho_j^{(0)}(\mathbf{x}') \right) h_{ij}^{\text{wall}}(\mathbf{x}') \psi_{ij}^D(\mathbf{x}, \mathbf{x}') d\mathbf{x}' \\ & + \text{sgn} \left(\frac{\epsilon - \epsilon_{\text{wall}}}{\epsilon + \epsilon_{\text{wall}}} \right) \sum_j \int \left(\frac{1}{4} \rho_j(\mathbf{x}') + \frac{1}{12} \rho_j^{(0)}(\mathbf{x}') \right) h_{ij}^D(\mathbf{x}^*, \mathbf{x}') \psi_{ij}^D(\mathbf{x}, \mathbf{x}') d\mathbf{x} \\ & + \frac{1}{2} \psi_{ii}^D(\mathbf{x}, \mathbf{x}) \end{aligned} \quad (19)$$

where ϕ_D is the solution of the Poisson equation with the ion density profiles at their image charge locations and with corresponding reduced charge.

2.2 Single planar dielectric interface

If the dielectric boundary is a single planar interface at $x = 0$ with dielectric constant ϵ where the ions are and ϵ_{wall} behind the wall (where no ions are), then

$$\psi_{ij}^D(\mathbf{x}, \mathbf{x}') = \psi_{ij}^D(x + x', y - y', z - z') \quad (20)$$

$$= \frac{z_i z_j e^2}{4\pi\epsilon\epsilon_0} \frac{\epsilon - \epsilon_{\text{wall}}}{\epsilon + \epsilon_{\text{wall}}} \frac{1}{\sqrt{(x + x')^2 + (y - y')^2 + (z - z')^2}} \quad (21)$$

where $\mathbf{x} = (x, y, z)$ and similarly for \mathbf{x}' . The densities have planar symmetry so that $\rho_j(\mathbf{x}') = \rho_j(x')$. Then

$$\begin{aligned} & \int \rho_j(x') \left(\iint h_{ij}^{\text{ion}}(\mathbf{x}, \mathbf{x}') \psi_{ij}^D(\mathbf{x}, \mathbf{x}') dy' dz' \right) dx' \\ & = \int \rho_j(x') \left(\iint h_{ij}^{\text{ion}}(x - x', \sqrt{u^2 + v^2}) \psi_{ij}^D(x + x', \sqrt{u^2 + v^2}) du dv \right) dx' \end{aligned} \quad (22)$$

$$= 2\pi \int \rho_j(x') \left(\int_0^\infty w h_{ij}^{\text{ion}}(x - x', w) \psi_{ij}^D(x + x', w) dw \right) dx' \quad (23)$$

$$= \frac{z_i z_j e^2}{2\epsilon\epsilon_0} \frac{\epsilon - \epsilon_{\text{wall}}}{\epsilon + \epsilon_{\text{wall}}} \int \rho_j(x') \left(\int_0^\infty h_{ij}^{\text{ion}}(x - x', w) \frac{w}{\sqrt{(x + x')^2 + w^2}} dw \right) dx' \quad (24)$$

because

$$\psi_{ij}^D(a, w) = \frac{z_i z_j e^2}{4\pi\epsilon\epsilon_0} \frac{\epsilon - \epsilon_w}{\epsilon + \epsilon_w} \frac{1}{\sqrt{a^2 + w^2}}. \quad (25)$$

We must therefore evaluate the integral

$$\int_0^\infty h_{ij}^{\text{ion}}(x - x', w) \frac{w}{\sqrt{(x + x')^2 + w^2}} dw = \int_{|x+x'|}^\infty h_{ij}^{\text{ion}}\left(x - x', \sqrt{v^2 - (x + x')^2}\right) dv \quad (26)$$

where

$$v = \sqrt{(x + x')^2 + w^2}. \quad (27)$$

2.3 Ion TCF

For the ion TCF, in Eq. (11) we define

$$h_{ij}^{\text{ion}}(\mathbf{x}, \mathbf{x}') = \begin{cases} \chi_i(\mathbf{x}) h_{ij}^{\text{bulk}}(|\mathbf{x} - \mathbf{x}'|) & \text{if } |\mathbf{x} - \mathbf{x}'| \geq R_{ij} \\ -1 & \text{otherwise.} \end{cases} \quad (28)$$

Now we make the ansatz that the bulk TCF has the form of a Yukawa potential $Y(r; a, b)$, similar to that of the linearized Poisson-Boltzmann solution, but in this case the coefficients may be fit to, for example, the solution of the nonlinearized Poisson-Boltzmann equation:

$$h_{ij}^{\text{bulk}}(r) \approx H_{ij}(s, w) \equiv Y\left(s, w; c_1^{ij}, c_2^{ij}, R_{ij}\right) \quad (29)$$

$$= \frac{c_1^{ij}}{\sqrt{s^2 + w^2}} \exp\left(\frac{R_{ij} - \sqrt{s^2 + w^2}}{c_2^{ij}}\right) \quad (30)$$

where R_{ij} is the contact radius of the two ion species and the c_k^{ij} are constants (either from LPB or fitted to the NPB solution).

Next we evaluate Eq. (26). For h_{ij}^{ion} , it is -1 when $|\mathbf{x} - \mathbf{x}'| < R_{ij}$ and the decaying function H_{ij} otherwise. For $|\mathbf{x} - \mathbf{x}'| < R_{ij}$, we must have

$$R_{ij}^2 > (x - x')^2 + w^2 \quad (31)$$

$$= (x - x')^2 + v^2 - (x + x')^2 \quad (32)$$

or

$$v^2 \leq R_{ij}^2 + 4xx'. \quad (33)$$

But, v is also bounded below because $w \geq 0$, so for $|\mathbf{x} - \mathbf{x}'| < R_{ij}$ we must have

$$(x + x')^2 \leq v^2 \leq R_{ij}^2 + 4xx'. \quad (34)$$

Therefore, if

$$|x + x'| \leq \sqrt{R_{ij}^2 + 4xx'}, \quad (35)$$

then

$$\begin{aligned} & \int_{|x+x'|}^{\infty} h_{ij}^{\text{ion}}\left(x - x', \sqrt{v^2 - (x + x')^2}\right) dv \\ &= - \int_{|x+x'|}^{\sqrt{R_{ij}^2 + 4xx'}} dv + \int_{\sqrt{R_{ij}^2 + 4xx'}}^{\infty} H_{ij}\left(x - x', \sqrt{v^2 - (x + x')^2}\right) dv \end{aligned} \quad (36)$$

$$\begin{aligned} &= |x + x'| - \sqrt{R_{ij}^2 + 4xx'} \\ &+ \int_{\sqrt{R_{ij}^2 + 4xx'}}^{\infty} H_{ij}\left(x - x', \sqrt{v^2 - (x + x')^2}\right) dv. \end{aligned} \quad (37)$$

Otherwise, if

$$|x + x'| > \sqrt{R_{ij}^2 + 4xx'}, \quad (38)$$

then

$$\int_{|x+x'|}^{\infty} h_{ij}^{\text{ion}}\left(x - x', \sqrt{v^2 - (x + x')^2}\right) dv = \int_{|x+x'|}^{\infty} H_{ij}\left(x - x', \sqrt{v^2 - (x + x')^2}\right) dv. \quad (39)$$

We can put these together by letting

$$m_{ij}(x, x') = \max \left\{ |x + x'|, \sqrt{R_{ij}^2 + 4xx'} \right\} \quad (40)$$

so that

$$\begin{aligned} & \int_{|x+x'|}^{\infty} h_{ij}^{\text{ion}} \left(x - x', \sqrt{v^2 - (x + x')^2} \right) dv \\ &= |x + x'| - m_{ij}(x, x') + \int_{m_{ij}(x, x')}^{\infty} H_{ij} \left(x - x', \sqrt{v^2 - (x + x')^2} \right) dv. \end{aligned} \quad (41)$$

This last integral is the first major bottleneck in the numerical calculation because of the $x - x'$ and $x + x'$ dependence of the integrand. This makes it nearly impossible to do in $O(N)$ time and generally in $O(N^2)$ time. $O(N^2)$ time is not useful for practical applications. For example, the profiles in Fig. 1 we done using $N = 128$ grid points and took ~2 minutes. For practical problems, at least $N = 1000$ is necessary, if not $N = 10000$. With $O(N^2)$ time, this would take ~200 minutes which is not practical. The last period of the grant spent significant portions of time to evaluate this integral efficiently, using various techniques from polynomial interpolation to Gaussian quadratures but none have—so far—been efficient enough for a practical real-world problem.

2.3.1 Scaling of ion TCF

By Eq. (13),

$$q_{ij}(\mathbf{x}) = z_j e \rho_j^{\text{bulk}} \int_{|\mathbf{x} - \mathbf{x}'| \geq R_{ij}} h_{ij}^{\text{ion}}(|\mathbf{x} - \mathbf{x}'|) e^{-V_j^{\text{ext}}(\mathbf{x}')/kT} d\mathbf{x}' \quad (42)$$

$$= 2\pi z_j e \rho_j^{\text{bulk}} \int e^{-V_j^{\text{ext}}(x')/kT} \left(\int_{M_{ij}(x-x')}^{\infty} w H_{ij}(x - x', w) dw \right) dx' \quad (43)$$

where

$$M_{ij}^2(x - x') = \max \left\{ R_{ij}^2 - (x - x')^2, 0 \right\} \quad (44)$$

because the lower bound for the radial coordinate w (in cylindrical coordinates) is $\sqrt{R_{ij}^2 - (x - x')^2}$ if $|x - x'| < R_{ij}$ and 0 when $x - x'$ is outside the contact sphere. Then

$$\begin{aligned} & \int_{M_{ij}(x-x')}^{\infty} w H_{ij}(x - x', w) dw \\ &= c_1^{ij} e^{R_c/c_2^{ij}} \int_{M_{ij}(x-x')}^{\infty} w \frac{1}{\sqrt{(x - x')^2 + w^2}} \exp \left(-\frac{\sqrt{(x - x')^2 + w^2}}{c_2^{ij}} \right) dw. \end{aligned} \quad (45)$$

The integral can be evaluated with the substitution

$$v = \sqrt{(x - x')^2 + w^2} \quad (46)$$

$$dv = \frac{w}{\sqrt{(x - x')^2 + w^2}} dw. \quad (47)$$

Then

$$\begin{aligned} & \int_{M_{ij}(x-x')}^{\infty} w \frac{1}{\sqrt{(x-x')^2 + w^2}} \exp\left(-\frac{\sqrt{(x-x')^2 + w^2}}{c_2^{ij}}\right) dw \\ &= \int_{\max\{R_{ij}, |x-x'|\}}^{\infty} \exp\left(-\frac{v}{c_2^{ij}}\right) dv \\ &= c_2^{ij} \exp\left(-\frac{\max\{R_{ij}, |x-x'|\}}{c_2^{ij}}\right) \end{aligned} \quad (48)$$

$$= c_2^{ij} \exp\left(-\frac{\max\{R_{ij}, |x-x'|\}}{c_2^{ij}}\right) \quad (49)$$

so that

$$q_{ij}(x) = 2\pi z_j e \rho_j^{\text{bulk}} c_1^{ij} c_2^{ij} e^{R_c^{ij}/c_2^{ij}} \int e^{-V_j^{\text{ext}}(x')/kT} \exp\left(-\frac{\max\{R_{ij}, |x-x'|\}}{c_2^{ij}}\right) dx' \quad (50)$$

$$= 2\pi z_j e \rho_j^{\text{bulk}} c_1^{ij} c_2^{ij} e^{R_c^{ij}/c_2^{ij}} \int_{R_j+x_w}^{\infty} \exp\left(-\frac{\max\{R_{ij}, |x-x'|\}}{c_2^{ij}}\right) dx' \quad (51)$$

$$= 2\pi z_j e \rho_j^{\text{bulk}} c_1^{ij} c_2^{ij} e^{R_c^{ij}/c_2^{ij}} \int_{R_j}^{\infty} \exp\left(-\frac{\max\{R_{ij}, |x_0-x'_0|\}}{c_2^{ij}}\right) dx'_0 \quad (52)$$

where x_w is the x location of the wall and

$$x_0 = x - x_w \quad (53)$$

is the distance of x from the wall, with a similar definition for x'_0 .

To evaluate $\max\{R_{ij}, |x_0-x'_0|\}$, consider that $|x_0-x'_0| < R_{ij}$ is equivalent to

$$x_0 - R_{ij} < x'_0 < x_0 + R_{ij}. \quad (54)$$

For the ions, $x_0 > 0$ so that

$$\begin{aligned} & \int_{R_j}^{\infty} \exp\left(-\frac{\max\{R_{ij}, |x_0-x'_0|\}}{c_2^{ij}}\right) dx'_0 \\ &= \exp\left(-\frac{R_{ij}}{c_2^{ij}}\right) \int_{\max\{x_0-R_{ij}, R_j\}}^{x_0+R_{ij}} dx'_0 + \int_{x_0+R_{ij}}^{\infty} \exp\left(-\frac{|x_0-x'_0|}{c_2^{ij}}\right) dx'_0 \end{aligned} \quad (55)$$

$$\begin{aligned} & + \int_{R_j}^{\max\{x_0-R_{ij}, R_j\}} \exp\left(-\frac{|x_0-x'_0|}{c_2^{ij}}\right) dx'_0 \\ &= \exp\left(-\frac{R_{ij}}{c_2^{ij}}\right) (x_0 + R_{ij} - \max\{x_0 - R_{ij}, R_j\}) + \int_{R_{ij}}^{\infty} \exp\left(-\frac{s'}{c_2^{ij}}\right) ds' \\ & + \int_{R_j-x_0}^{\max\{x_0-R_{ij}, R_j\}-x_0} \exp\left(-\frac{|s'|}{c_2^{ij}}\right) ds'. \end{aligned} \quad (56)$$

The last integral can be evaluated as follows:

$$\begin{aligned} & \int_{R_j-x_0}^{\max\{x_0-R_{ij}, R_j\}-x_0} \exp\left(-\frac{|s'|}{c_2^{ij}}\right) ds' \\ &= \begin{cases} \int_{R_j-x_0}^{-R_{ij}} \exp\left(-\frac{|s'|}{c_2^{ij}}\right) ds' & \text{if } \max\{x_0-R_{ij}, R_j\} = x_0-R_{ij} \\ 0 & \text{otherwise} \end{cases} \end{aligned} \quad (57)$$

$$= \begin{cases} \int_{R_{ij}}^{x_0-R_j} \exp\left(-\frac{s'}{c_2^{ij}}\right) ds' & \text{if } \max\{x_0-R_{ij}, R_j\} = x_0-R_{ij} \\ 0 & \text{otherwise.} \end{cases} \quad (58)$$

Then

$$\int_{R_j}^{\infty} \exp\left(-\frac{\max\{R_{ij}, |x_0-x'_0|\}}{c_2^{ij}}\right) dx'_0 \quad (59)$$

$$= \exp\left(-\frac{R_{ij}}{c_2^{ij}}\right) (x_0 + R_{ij} - \max\{x_0-R_{ij}, R_j\}) + c_2^{ij} \exp\left(-\frac{R_{ij}}{c_2^{ij}}\right) \quad (60)$$

$$+ c_2^{ij} \begin{cases} \exp\left(-\frac{R_{ij}}{c_2^{ij}}\right) - \exp\left(-\frac{x_0-R_j}{c_2^{ij}}\right) & \text{if } \max\{x_0-R_{ij}, R_j\} = x_0-R_{ij} \\ 0 & \text{otherwise} \end{cases} \quad (61)$$

which defines $q_{ij}(x)$ through Eq. (52).

2.4 Dielectric TCF

For the dielectric TCF h_{ij}^D , we use an LPB approach around each surface charge element σ at \mathbf{s} . Specifically, consider an ion of species i at \mathbf{x} that induces a surface charge profile $\sigma_i(\mathbf{s}; \mathbf{x})$ for \mathbf{s} on the dielectric interface S . Next, we assume that the ions accumulating around this surface charge element make a potential

$$\phi_i(\mathbf{s}, \mathbf{x}'; \mathbf{x}) \approx \frac{a_i(\mathbf{x})}{4\pi\epsilon_0} \frac{\sigma_i(\mathbf{s}; \mathbf{x})}{|\mathbf{s} - \mathbf{x}'|} \exp\left(-\frac{|\mathbf{s} - \mathbf{x}'|}{\lambda}\right) \quad (62)$$

where Y is the Yukawa potential with characteristic lengthscale (the Debye length)

$$\lambda^2 = \sqrt{\frac{\epsilon\epsilon_0 kT}{e^2 \sum_j z_j^2 \rho_j^{\text{bath}}}} \quad (63)$$

and with an as-yet-undetermined coefficient $a_i(\mathbf{x})$. Because the LPB is additive,

$$\Phi_i(\mathbf{x}'; \mathbf{x}) = \int_S \phi_i(\mathbf{s}, \mathbf{x}'; \mathbf{x}) ds \quad (64)$$

$$= \frac{a_i(\mathbf{x})}{4\pi\epsilon_0} \int_S \frac{\sigma_i(\mathbf{s}; \mathbf{x})}{|\mathbf{s} - \mathbf{x}'|} \exp\left(-\frac{|\mathbf{s} - \mathbf{x}'|}{\lambda}\right) ds. \quad (65)$$

With the LPB approximation,

$$h_{ij}^D(\mathbf{x}, \mathbf{x}') \approx \begin{cases} -\frac{z_j e}{kT} \Phi_i(\mathbf{x}'; \mathbf{x}) & |\mathbf{x} - \mathbf{x}'| \geq R_{ij} \\ 0 & |\mathbf{x} - \mathbf{x}'| < R_{ij}. \end{cases} \quad (66)$$

In the planar geometry,

$$\begin{aligned}
\Phi_i(\mathbf{x}'; \mathbf{x}) &= \int_S \frac{\sigma_i(\mathbf{s}; \mathbf{x})}{|\mathbf{s} - \mathbf{x}'|} \exp\left(-\frac{|\mathbf{s} - \mathbf{x}'|}{\lambda}\right) d\mathbf{s} \\
&= a_i(\mathbf{x}) \frac{1}{2\pi} \frac{\epsilon - \epsilon_{\text{wall}}}{\epsilon + \epsilon_{\text{wall}}} \frac{z_i e}{4\pi\epsilon\epsilon_0} \\
&\quad \times \int_{-\infty}^{\infty} \int_{-\infty}^{\infty} \frac{x_0}{\left(x_0^2 + (y - s_y)^2 + (z - s_z)^2\right)^{3/2}} \frac{\exp\left[-\left((x'_0)^2 + (y' - s_y)^2 + (z' - s_z)^2\right)^{1/2} / \lambda\right]}{\left((x'_0)^2 + (y' - s_y)^2 + (z' - s_z)^2\right)^{1/2}} ds_y ds_z.
\end{aligned} \tag{67}$$

This double integral can be simplified:

$$\begin{aligned}
&\int_{-\infty}^{\infty} \int_{-\infty}^{\infty} \frac{x_0}{\left(x_0^2 + (y - s_y)^2 + (z - s_z)^2\right)^{3/2}} \frac{\exp\left[-\left((x'_0)^2 + (y' - s_y)^2 + (z' - s_z)^2\right)^{1/2} / \lambda\right]}{\left((x'_0)^2 + (y' - s_y)^2 + (z' - s_z)^2\right)^{1/2}} ds_y ds_z \\
&= \int_{-\infty}^{\infty} \int_{-\infty}^{\infty} \frac{x_0}{\left(x_0^2 + (u_y + Y)^2 + (u_z + Z)^2\right)^{3/2}} \frac{\exp\left[-\left((x'_0)^2 + u_y^2 + u_z^2\right)^{1/2} / \lambda\right]}{\left((x'_0)^2 + u_y^2 + u_z^2\right)^{1/2}} du_y du_z
\end{aligned} \tag{68}$$

$$= \int_0^{\infty} \int_0^{2\pi} \frac{x_0 r}{\left(x_0^2 + (r \cos(\theta) + Y)^2 + (r \sin(\theta) + Z)^2\right)^{3/2}} \frac{\exp\left[-\left((x'_0)^2 + r^2\right)^{1/2} / \lambda\right]}{\left((x'_0)^2 + r^2\right)^{1/2}} d\theta dr \tag{69}$$

$$= x_0 \int_0^{\infty} r \left(\int_0^{2\pi} \frac{d\theta}{\left(x_0^2 + (r \cos(\theta) + Y)^2 + (r \sin(\theta) + Z)^2\right)^{3/2}} \right) \frac{\exp\left[-\left((x'_0)^2 + r^2\right)^{1/2} / \lambda\right]}{\left((x'_0)^2 + r^2\right)^{1/2}} dr \tag{70}$$

where

$$u_y = s_y - y' = r \cos(\theta) \tag{71}$$

$$u_z = s_z - z' = r \sin(\theta) \tag{72}$$

with $Y = y' - y$ and $Z = z' - z$. With the substitution

$$\theta = \tau + c \tag{73}$$

$$\tan(c) = \frac{a}{b}, \tag{74}$$

one can show that

$$\int_0^{2\pi} f(a \sin(\theta) + b \cos(\theta)) d\theta = \int_0^{2\pi} f\left(\sqrt{a^2 + b^2} \cos(\tau)\right) d\tau \tag{75}$$

$$= 2 \int_0^{\pi} f\left(\sqrt{a^2 + b^2} \cos(\tau)\right) d\tau. \tag{76}$$

Therefore,

$$\int_0^{2\pi} \frac{d\theta}{(x_0^2 + r^2 + Y^2 + Z^2 + 2r(Y \cos(\theta) + Z \sin(\theta)))^{3/2}} = 2 \int_0^\pi \frac{d\tau}{(x_0^2 + r^2 + w^2 + 2rw \cos(\tau))^{3/2}} \quad (77)$$

$$= \frac{2}{(x_0^2 + r^2 + w^2)^{3/2}} \int_0^\pi \frac{d\tau}{\left(1 + \frac{2rw}{x_0^2 + r^2 + w^2} \cos(\tau)\right)^{3/2}} \quad (78)$$

and finally

$$\Phi_i(\mathbf{x}'; \mathbf{x}) = \Phi_i(x_0, x'_0, w) \quad (79)$$

$$= a_i(\mathbf{x}) \frac{\epsilon - \epsilon_{\text{wall}}}{\epsilon + \epsilon_{\text{wall}}} \frac{z_i e}{4\pi\epsilon\epsilon_0} x_0 \int_0^\infty \frac{r}{(x_0^2 + r^2 + w^2)^{3/2}} \tau \left(\frac{2rw}{x_0^2 + r^2 + w^2} \right) \frac{\exp\left[-\left((x'_0)^2 + r^2\right)^{1/2}/\lambda\right]}{\left((x'_0)^2 + r^2\right)^{1/2}} dr \quad (80)$$

where

$$\tau(p) = \frac{1}{\pi} \int_0^\pi \frac{d\tau'}{(1 + p \cos(\tau'))^{3/2}}. \quad (81)$$

For $0 \leq p \leq 1$, the function $f(p)$ can be well approximated by

$$\tau(p) \approx \frac{1 - 0.962278036p + 0.675857675p^2 - 0.262241607p^3}{1 - p}. \quad (82)$$

Then

$$\mu_i^D(x) = \sum_j \int \rho_j^\#(x') \left(\iint h_{ij}^D(\mathbf{x}, \mathbf{x}') \psi_{ij}^D(\mathbf{x}, \mathbf{x}') dy' dz' \right) dx' \quad (83)$$

$$\approx -\frac{e}{kT} \sum_j z_j \int \rho_j^\#(x') \left(\iint \Phi_i(\mathbf{x}'; \mathbf{x}) \psi_{ij}^D(\mathbf{x}, \mathbf{x}') dy' dz' \right) dx' \quad (84)$$

$$= -2\pi \frac{e}{kT} \sum_j z_j \int \rho_j^\#(x') \left(\int_{\sqrt{(x_0 - x'_0)^2 + w^2} > R_{ij}} w \Phi_i(x_0, x'_0, w) \psi_{ij}^D(x + x', w) dw \right) dx'. \quad (85)$$

This last integral is the second major bottleneck in the numerical calculation because of the x and x' dependence of the integrand and because for each x and x' , $\Phi_i(x_0, x'_0, w)$ must be calculated in another difficult integral.

2.4.1 Scaling the dielectric TCF

Like with the ion TCF, we require charge neutrality of the ions around the dielectric induced charge:

$$-\epsilon \int_S \sigma_i(\mathbf{s}; \mathbf{x}) d\mathbf{s} = e \sum_j z_j \rho_j^{\text{bath}} \int h_{ij}^D(\mathbf{x}, \mathbf{x}') e^{-V_j(\mathbf{x}')/kT} d\mathbf{x}'. \quad (86)$$

For the planar case, we know that

$$\epsilon \int_S \sigma_i(\mathbf{s}; \mathbf{x}) d\mathbf{s} = z_i e \frac{\epsilon - \epsilon_w}{\epsilon + \epsilon_w}. \quad (87)$$

From above we have that

$$h_{ij}^D(\mathbf{x}, \mathbf{x}') = \begin{cases} -\frac{z_j e}{kT} \Phi_i(\mathbf{x}'; \mathbf{x}) & |\mathbf{x} - \mathbf{x}'| \geq R_{ij} \\ 0 & |\mathbf{x} - \mathbf{x}'| < R_{ij} \end{cases} \quad (88)$$

so we wind up with

$$-\epsilon \int_S \sigma_i(\mathbf{s}; \mathbf{x}) d\mathbf{s} = e \sum_j z_j \rho_j^{\text{bath}} \int h_{ij}^D(\mathbf{x}, \mathbf{x}') e^{-V_j(\mathbf{x}')/kT} d\mathbf{x}' \quad (89)$$

$$= -\frac{e^2}{kT} \sum_j z_j^2 \rho_j^{\text{bath}} \int_{|\mathbf{x}-\mathbf{x}'| \geq R_{ij}} \Phi_i(\mathbf{x}'; \mathbf{x}) e^{-V_j(\mathbf{x}')/kT} d\mathbf{x}' \quad (90)$$

$$= -2\pi \frac{e^2}{kT} \sum_j z_j^2 \rho_j^{\text{bath}} \int_{-\infty}^{\infty} e^{-V_j(x'_0)/kT} \int_{\sqrt{(x_0-x'_0)^2+w^2} > R_{ij}} w \Phi_i(x_0, x'_0, w) dw dx'_0 \quad (91)$$

$$= -2\pi \frac{e^2}{kT} \sum_j z_j^2 \rho_j^{\text{bath}} \int_{R_j}^{\infty} \int_{M_{ij}(x_0-x'_0)}^{\infty} w \Phi_i(x_0, x'_0, w) dw dx'_0 \quad (92)$$

$$= -2\pi \frac{e^2}{kT} \sum_j z_j^2 \rho_j^{\text{bath}} \int_{R_j}^{\infty} \int_0^{\infty} w \Phi_i(x_0, x'_0, w) dw dx'_0 \quad (93)$$

$$+ 2\pi \frac{e^2}{kT} \sum_j z_j^2 \rho_j^{\text{bath}} \int_{R_j}^{\infty} \int_0^{M_{ij}(x_0-x'_0)} w \Phi_i(x_0, x'_0, w) dw dx'_0 \quad (94)$$

where

$$M_{ij}^2(x_0 - x'_0) = \max \left\{ R_{ij}^2 - (x_0 - x'_0)^2, 0 \right\}. \quad (95)$$

For the first integral, we use the fact that

$$\int_0^{\infty} w \frac{r}{(x_0^2 + r^2 + w^2)^{3/2}} \tau \left(\frac{2rw}{x_0^2 + r^2 + w^2} \right) dw = \frac{r}{x_0} \quad (96)$$

to determine that

$$-2\pi \frac{e^2}{kT} \sum_j z_j^2 \rho_j^{\text{bath}} \int_{R_j}^{\infty} \int_0^{\infty} w \Phi_i(x_0, x'_0, w) dw dx'_0 \quad (97)$$

$$= -2\pi \frac{e^2}{kT} \sum_j z_j^2 \rho_j^{\text{bath}} \int_{R_j}^{\infty} a_i(\mathbf{x}) \frac{\epsilon - \epsilon_{\text{wall}}}{\epsilon + \epsilon_{\text{wall}}} \frac{z_i e}{4\pi \epsilon \epsilon_0} x_0 \int_0^{\infty} \frac{r}{x_0} \frac{\exp \left[- \left((x'_0)^2 + r^2 \right)^{1/2} / \lambda \right]}{\left((x'_0)^2 + r^2 \right)^{1/2}} dr dx'_0 \quad (98)$$

$$= -2\pi \frac{e^2}{kT} \sum_j z_j^2 \rho_j^{\text{bath}} \int_{R_j}^{\infty} a_i(\mathbf{x}) \frac{\epsilon - \epsilon_{\text{wall}}}{\epsilon + \epsilon_{\text{wall}}} \frac{z_i e}{4\pi \epsilon \epsilon_0} \int_0^{\infty} r \frac{\exp \left[- \left((x'_0)^2 + r^2 \right)^{1/2} / \lambda \right]}{\left((x'_0)^2 + r^2 \right)^{1/2}} dr dx'_0 \quad (99)$$

$$= -2\pi \frac{e^2}{kT} \sum_j z_j^2 \rho_j^{\text{bath}} \int_{R_j}^{\infty} a_i(\mathbf{x}) \frac{\epsilon - \epsilon_{\text{wall}}}{\epsilon + \epsilon_{\text{wall}}} \frac{z_i e}{4\pi \epsilon \epsilon_0} \int_{x'_0}^{\infty} \exp[-u/\lambda] du dx'_0 \quad (100)$$

$$= -2\pi \frac{e^2}{kT} a_i(x) \frac{\epsilon - \epsilon_{\text{wall}}}{\epsilon + \epsilon_{\text{wall}}} \frac{z_i e}{4\pi \epsilon \epsilon_0} \lambda \sum_j z_j^2 \rho_j^{\text{bath}} \int_{R_j}^{\infty} \exp \left(-\frac{x'_0}{\lambda} \right) dx'_0 \quad (101)$$

$$= -2\pi \frac{e^2}{kT} a_i(x) \frac{\epsilon - \epsilon_{\text{wall}}}{\epsilon + \epsilon_{\text{wall}}} \frac{z_i e}{4\pi \epsilon \epsilon_0} \lambda^2 \sum_j z_j^2 \rho_j^{\text{bath}} \exp \left(-\frac{R_j}{\lambda} \right). \quad (102)$$

For the second integral,

$$2\pi \frac{e^2}{kT} \sum_j z_j^2 \rho_j^{\text{bath}} \int_{R_j}^{\infty} \int_0^{M_{ij}(x_0-x'_0)} w \Phi_i(x_0, x'_0, w) dw dx'_0 \quad (103)$$

$$= 2\pi \frac{e^2}{kT} a_i(x) \frac{\epsilon - \epsilon_{\text{wall}}}{\epsilon + \epsilon_{\text{wall}}} \frac{z_i e}{4\pi \epsilon \epsilon_0} x_0 \sum_j z_j^2 \rho_j^{\text{bath}} f_{ij}(x_0) \frac{\exp\left[-\left((x'_0)^2 + r^2\right)^{1/2}/\lambda\right]}{\left((x'_0)^2 + r^2\right)^{1/2}} dr dx'_0 \quad (104)$$

where

$$f_{ij}(x_0) = \int_{R_j}^{\infty} \int_0^{\infty} \left[\int_0^{M_{ij}(x_0-x'_0)} w \frac{r}{(x_0^2 + r^2 + w^2)^{3/2}} \tau\left(\frac{2rw}{x_0^2 + r^2 + w^2}\right) dw \right] \frac{\exp\left[-\left((x'_0)^2 + r^2\right)^{1/2}/\lambda\right]}{\left((x'_0)^2 + r^2\right)^{1/2}} dr dx'_0 \quad (105)$$

which must be determined numerically. This is simplified because

$$M_{ij}(x_0 - x'_0) = \begin{cases} \sqrt{R_{ij}^2 - (x_0 - x'_0)^2} & |x_0 - x'_0| < R_{ij} \\ 0 & |x_0 - x'_0| \geq R_{ij} \end{cases} \quad (106)$$

which implies that

$$x_0 - R_{ij} < x'_0 < x_0 + R_{ij} \quad (107)$$

and

$$f_{ij}(x_0) = \int_{\max\{R_j, x_0 - R_{ij}\}}^{x_0 + R_{ij}} \int_0^{\infty} \left[\int_0^{\sqrt{R_{ij}^2 - (x_0 - x'_0)^2}} \frac{w}{(x_0^2 + r^2 + w^2)^{3/2}} \tau\left(\frac{2rw}{x_0^2 + r^2 + w^2}\right) dw \right] \times r \frac{\exp\left[-\left((x'_0)^2 + r^2\right)^{1/2}/\lambda\right]}{\left((x'_0)^2 + r^2\right)^{1/2}} dr dx'_0. \quad (108)$$

The scaling factor is then

$$a_i(x) = \frac{2\epsilon\epsilon_0 kT}{e^2} \frac{1}{\lambda^2 \sum_j z_j^2 \rho_j^{\text{bath}} \exp\left(-\frac{R_j}{\lambda}\right) - x_0 \sum_j z_j^2 \rho_j^{\text{bath}} f_{ij}(x_0)}. \quad (109)$$

2.5 Wall component

For the wall component,

$$\sum_j \int \left(\frac{1}{3} \rho_j(\mathbf{x}') + \frac{1}{6} \rho_j^{(0)}(\mathbf{x}') \right) h_{ij}^{\text{wall}}(\mathbf{x}') \psi_{ij}^D(\mathbf{x}, \mathbf{x}') d\mathbf{x}' \quad (110)$$

$$= \sum_j \int_{|\mathbf{x} - \mathbf{x}'| \geq R_{ij}} \rho_j^{\#}(\mathbf{x}') \left(\frac{\rho_j^{(0)}(\mathbf{x}')}{\rho_j^{\text{bath}}} - 1 \right) \psi_{ij}^D(\mathbf{x}, \mathbf{x}') d\mathbf{x}' \quad (111)$$

$$= \sum_j \int \rho_j^{\#}(\mathbf{x}') \left(\frac{\rho_j^{(0)}(\mathbf{x}')}{\rho_j^{\text{bath}}} - 1 \right) \psi_{ij}^D(\mathbf{x}, \mathbf{x}') d\mathbf{x}' \quad (112)$$

$$- \sum_j \int_{|\mathbf{x} - \mathbf{x}'| < R_{ij}} \rho_j^{\#}(\mathbf{x}') \left(\frac{\rho_j^{(0)}(\mathbf{x}')}{\rho_j^{\text{bath}}} - 1 \right) \psi_{ij}^D(\mathbf{x}, \mathbf{x}') d\mathbf{x}'. \quad (113)$$

The first integral is the solution of a Poisson equation similar to ϕ_D above. For the second integral,

$$\sum_j \int_{|\mathbf{x}-\mathbf{x}'| < R_{ij}} \rho_j^\#(\mathbf{x}') \left(\frac{\rho_j^{(0)}(\mathbf{x}')}{\rho_j^{\text{bath}}} - 1 \right) \psi_{ij}^D(\mathbf{x}, \mathbf{x}') d\mathbf{x}' \quad (114)$$

$$= 2\pi \sum_j \int \rho_j^\#(x') \left(\frac{\rho_j^{(0)}(x')}{\rho_j^{\text{bath}}} - 1 \right) \left(\int_0^{M_{ij}(x_0-x'_0)} w \psi_{ij}^D(x, x', w) dw \right) dx' \quad (115)$$

$$= 2\pi \sum_j \int_{x-R_{ij}}^{x+R_{ij}} \rho_j^\#(x') \left(\frac{\rho_j^{(0)}(x')}{\rho_j^{\text{bath}}} - 1 \right) \left(\int_0^{\sqrt{R_{ij}^2-(x-x')^2}} w \psi_{ij}^D(x, x', w) dw \right) dx' \quad (116)$$

$$= \frac{z_i e^2}{2\epsilon\epsilon_0} \frac{\epsilon - \epsilon_w}{\epsilon + \epsilon_w} \sum_j z_j \int_{x-R_{ij}}^{x+R_{ij}} \rho_j^\#(x') \left(\frac{\rho_j^{(0)}(x')}{\rho_j^{\text{bath}}} - 1 \right) \left(\sqrt{R_{ij}^2 + 4x_0x'_0} - (x_0 + x'_0) \right) dx'. \quad (117)$$

2.6 Toward an efficient numerical implementation

For the *Journal of Physical Chemistry Letters* paper, the dielectric DFT equations were solved using a specially written program developed by the PI. However, this code is very inefficient, not practical for real problems, and not accessible to other scientists. Therefore, the PI rewrote the entire DFT code (dielectric and older components) using the platform of *Mathematica*. Mathematica was chosen because it is widely available for all computer platforms (Windows, Mac, Linux) and has excellent support and upgrades. Mathematica also includes a huge number of built-in functions that make programming significantly easier.

Since the end of Year 1, much time has been spent rewriting the PI's original DFT code (the part without the dielectric functional) in Mathematica. This work is nearly done. Part of the grant went to supporting an undergraduate student (Jordan Hoffmann, Johns Hopkins University) to put the code through its paces by doing calculations on nanofluidic devices (see below). This very rigorous testing proved necessary, with Jordan finding many places of improvement for the code (e.g., systems for which it was slow, systems for which it did not find an answer, and on rare occasions systems for which it produced an incorrect answer).

The continuing work, beyond the completion of the grant, is the deriving and implementation of an efficient numerical algorithm for the bottleneck areas identified above.

3 Technical Details of FMM Implementation (written by Dr. Matt Knepley)

3.1 FMM Overview

The fast multipole method (FMM) is an algorithm that accelerates the application of certain integral operators, namely those satisfying the Calderón-Zygmund conditions. After discretization, this application may be expressed in the form

$$f(y_j) = \sum_{i=1}^N u(x_i) \mathbb{K}(y_j, x_i). \quad (118)$$

Naively, if we have N source points $\{x_i\}$ for the field u , and N target points $\{y_j\}$ for the field f , this summation would require $\mathcal{O}(N^2)$ operations. FMM allows us to reduce the computational complexity to $\mathcal{O}(N)$, which is essential for the operation of our DFT solves. This acceleration is accomplished by using a hierarchical partition of space into a tree structure. This tree structure allows efficient queries for points separations so that we can insert approximations for the kernel action at appropriate points.

We use a diagram of the tree structure to illustrate the whole algorithm in one picture (Figure 2). The importance of this bird's eye view is that it relates the algorithm computations to the data structure used by our FMM, and it will prove to be very useful when we discuss the parallel version that we have developed.

After the spatial decomposition stage, the FMM can be summarized in three stages: *upward sweep*, *downward sweep*, and *evaluation step*. In the *upward sweep*, the objective is to build the multipole expansions (ME s) for each node of the tree. The ME s are built first at the deepest level, level L , and then translated to the center of the parent nodes. This is illustrated in Figure 2 by the black arrows going up from the nodes on the left side of the tree (the process is of course performed for the whole tree). Thus, the ME s at the higher levels do not have to be computed from the particles, they are computed from the ME s of the child nodes. In the *downward sweep* of the tree, first the ME s are transformed into local expansions (LE s) for all the boxes in the *interaction list* —a process represented by the dashed red-colored arrows in Figure 2. For a given cell, the interaction list corresponds to the cells of the same level that are in the far field, but which are not in the interaction list of its parent cell. Once the ME s have been translated into LE s, the LE s of upper levels are translated to the centers of child cells, and their influence is added up to obtain the complete far domain influence for each box at the leaf level of the tree. This process is represented by the dashed blue-colored arrows going down the right side of the tree in Figure 2. At the end of the *downward sweep*, each box will have an LE that represents the complete far-field for the box. Finally, at the *evaluation step*, for every particle on every node at the deepest level of the tree, the total field is evaluated by adding the near-field and far-field contributions. The near field of the particles in a given cell is obtained by directly computing the interactions between all the particles in the near domain of the box. The far field of the particles is obtained by evaluating the LE of the box at each particle location.

3.2 Parallel Strategy

PetFMM is a parallel implementation of the FMM algorithm designed to be portable, extensible, scalable, and easily maintained [2]. The code base is quite small, and the parallel execution completely reuses the serial code, simplifying testing and optimization. The goal of our parallel strategy is to achieve an optimal distribution of the computational work among processes at runtime with a minimal communication overhead, and in this sense is *dynamic load balancing*.

We partition work according to subtrees of the original FMM tree. An important element of our parallel strategy is that partitioning are carried out automatically by an optimization tool, without intervention of the user. This is an alternative to the popular *space-filling curve* methods for parallel partitioning, which were first used for tree-codes in [7], and continue to be the prevalent method in both tree-codes and FMM implementations. Experiments reported in [6] using space-filling curve partitions for 200,000 particles in 12 processors, showed that elapsed wall-clock times for each processor varied between 60 and 140 seconds (as this work was before the time of multi-core processors, we keep the terminology “processor” rather than “process”). Thus, these experiments provide clear evidence that a uniform data partition via space-filling curve methods can result in considerable load imbalance, which we eliminate.

Our strategy for parallelization provides dynamic load balancing through an *optimization* procedure, based on a model of work and communications for the algorithm. We utilize the tree structure associated with the hierarchical decomposition of the domain in order to decompose the FMM into subtrees, for which the computational model has been developed. Notice that the tree structure has many roles: it is used as a space partitioner for the particles, it organizes the storage for the multipole expansions and local expansions, and it indicates the relations between nodes in the same level of the tree (whether two nodes are from the local domain list or the interaction list).

We apply a sub-division of the computations by cutting the d -dimensional tree at a certain level k , as shown in Figure 4. This procedure creates a *root* tree, that contains the first k levels of the original tree, and 2^{dk} *local* trees, each corresponding to one of the lower branches of the original tree. One key point when partitioning the tree is to obtain more subtrees than the number of available processes, so that work can be evenly distributed across the processes.

In the bird’s eye view of the whole algorithm, data and computations were related to nodes of the tree structure. When partitioning the tree representation into subtrees, computations that require data from different nodes of the partitioned tree might access data from several different partitions. If this is the case, communication between subtrees will happen as illustrated in Figure 3. By relating computations to nodes

of the tree, the work carried out by each subtree and the communication between different subtrees can be estimated, which is then used to optimally distribute the subtrees over available processes.

In order to assign subtrees to processes, we build a *graph representation* from the partitioned tree, as illustrated on Figure 4. The graph is assembled such that the vertices of the graph correspond to the subtrees and the edges correspond to communication between subtrees. Using the graph representation, we can assign weights to the vertices which are proportional to the amount of computational work performed by each subtree, and assign weights to the edges which are proportional to the amount of communication that happens between two subtrees.

The load balancing in the parallel algorithm is done by partitioning the weighted graph into as many parts as the number of available processes, and then assigning the subtrees to the processes according to the graph partitions. The problem of optimally partitioning the graph, such that the partitions are well-balanced and minimize the communication, is solved by the graph partitioning tool ParMetis [3, 4]. ParMetis is an open source graph partitioning tool, and is widely used in mesh partitioning applications. Figure 5 demonstrates the load balancing scheme at work. In an example computation, 1 million particles following a uniform distribution have been placed inside a square-shaped domain that is then hierarchically decomposed into a tree representation; the depth of the tree before partitioning is $L = 8$. The tree is then cut at level $k = 4$, resulting in 256 subtrees that are then distributed among 16 processes.

3.3 Electrostatics

In preparation, for the use of PetFMM for DFT electrostatics, we have developed a infrastructure for simple 3D electrostatics, as described in [13]. This was applied to a few large bioelectrotatic problems in order to evaluate accuracy and scalability.

Kernels for both single and double layer charge densities were developed for both multicore CPUs, such as the Intel Nehalem, and GPUs, such as the NVIDIA Tesla 1060C. Our novel *data-aware* queueing system allows the execution of either kernel type without changing the underlying FMM code. We have demonstrated good scalability for $N > 1000$ [14], which will be easily satisfied by our DFT calculations where we expect $N \cong 10^7$.

We have developed a new PETSc compatibility layer for PetFMM that will allow easy integration into the existing DFT code. Input and output data are organized in PETSc `Vec` objects, and `MatShell` wrappers for FMM evaluation allow it to be seamlessly used in all PETSc solvers.

To demonstrate the scalability on large problems, we use collections of randomly oriented lysozyme molecules arranged on a regular Cartesian grid, as a mimic of the Brownian dynamics calculations performed by McGuffee and Elcock [5] at each time step. One such collection, of 1000 proteins, is shown in Figure 6. The surface charge density for an isolated lysozyme molecule is plotted in Figure 7.

The largest simulation we have conducted consists of 10,648 molecules, where each surface was discretized into 102,486 elements. This calculation, which models more than 20 million atoms and possesses over one billion unknowns, required only approximately one minute per iteration on 512 nodes. The results of a more detailed scalability study of our code is shown in Figure 8. The present code can calculate the matrix-vector product of 6.4 billion elements in 57 seconds. This amounts to a performance of **34.6 TFlops**, as shown in Table 1

4 Implementation of the FMM method (written by Dr. Matt Knepley)

Dr Knepley is part of the grant through a subcontract. His role is to help develop a 3D version of the dielectric DFT code, which includes the components without dielectrics first. He is also responsible for developing fast algorithms for electrostatics and dielectrics that will be used in the code. He has made progress on both fronts in Year 2.

Table 1: Flops calculation

| Description | Equation | Value |
|----------------------------|------------------------------|-----------------------|
| Total number of points | N_p | 6.4×10^9 |
| Number of FMM cells | N_{cell} | 8^8 |
| Points per cell | N_p/N_{cell} | 381 |
| Interaction list | N_{list} | 27 |
| Operations per interaction | K | 30 |
| Time to solution | T | 57 |
| Total number of operations | $KN_pN_{list}N_p/N_{cell}/T$ | 3.46×10^{13} |

4.1 DFT Development

We have produced a three dimensional Density Functional Theory (DFT) code capable of simulating ionic liquids in generic geometries using both hard sphere and electrostatic interaction potentials. This code follows the development in [9] and [10]. It is based on the PETSc library [11], and in particular on the ability of PETSc to manage parallel multidimensional grids and Fast Fourier transforms (FFTs). With these building blocks, we could create a efficient, scalable code incorporating the key computational insights for DFT, detailed below.

The most important piece of technology introduced in our 3D DFT simulation is the use of spectral quadrature, which enables accurate conservation of Rosenfeld’s *fundamental measures*, as well as fast and accurate evaluation of RFD electrostatics. In one dimension, selection of a quadrature rule which accurately captures the volume of a ball, the surface of a sphere, and the directional average over the sphere is straightforward, even in the presence of discontinuities in the field being integrated. However, in three dimensions, this problem is intractable and discontinuities in the integrand, generally coming from a weighting functions, can result in $\mathcal{O}(1)$ errors in the result. The method of spectral quadrature moves the integral to Fourier space, using L_2 isometry, where both integrands are smooth, and can be readily integrated using traditional quadrature. Then the result, also smooth, is accurately moved to real space using the FFT.

As an example, when we evaluate the basis vectors n_α used in Rosenfeld’s formulation of the hard sphere interaction potential, we must convolve the density with a discontinuous weight function. Using the FFT produces unacceptable errors and non-conservation of the fundamental measures. Thus we use analytic Fourier transforms of the weight functions in order to stably evaluate each n_α , a simple example of spectral quadrature. This same method was applied to generate fast and accurate evaluations of the RFD reference density which using an averaging integral with a discontinuous weighting function. Moreover, the method of spectral quadrature was combined with a precise windowing method to reduce the RFD evaluation time from $\mathcal{O}(N^2)$ to $\mathcal{O}(N \log N)$, reducing runtime from weeks to hours.

The incorporation of the RFD model for local electrostatic correlations [10] as necessitated the introduction of another unknown field, Γ , the local inverse screening length. We have augmented the existing nonlinear algebraic solver to handle multiple fields. We have also introduced a nonlinear preconditioning step which provides a local approximate solution to Γ before using the Picard iteration to improve the density estimate. This was shown to provide much better convergence for the overall nonlinear system.

4.2 Electrostatics

The following descriptions of the algorithms will be implemented in the 3D DFT code by Dr. Knepley. They are generally applicable and therefore he is testing them on other systems because these systems have established benchmarks and compute faster than DFT. In this way, the implementation is much more efficient.

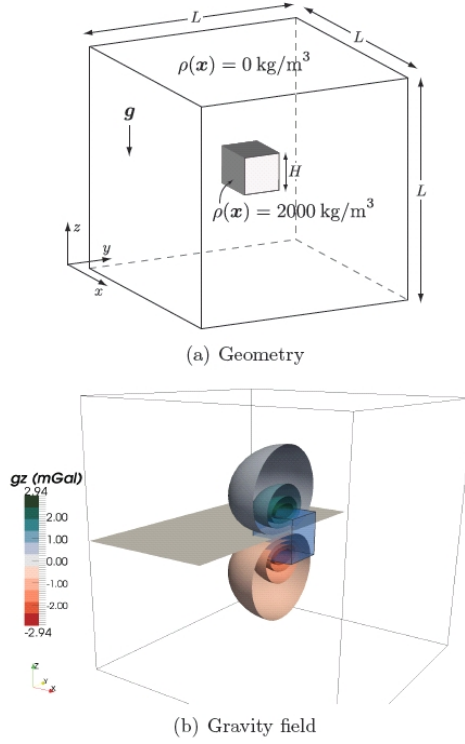


Figure 2: Synthetic model used thorough out the numerical experiments. (a) Domain and density anomaly and (b) the corresponding analytic gravity field g_z (mGal). The inclusion is indicated by the transparent blue cube. See text for dimensions of the domain and density anomaly.

4.2.1 Using FMM

In preparation, for the use of PetFMM for DFT electrostatics, we have developed an infrastructure for simple 3D electrostatics, as described in [12] and [13]. This was applied to a few large problems of gravity inversion and bioelectrotatics in order to evaluate accuracy and scalability. For three dimensions, we have improved the scalable partitioning, and now allow fully parallel input and output of the charge, potential, and electric field distribution. In Fig. 2, we show a density anomaly and the corresponding gravity field generated which we used to benchmark the parallel performance of PetFMM in three dimensions. In Table 3, we see that PetFMM shows good strong scaling up to 2000 processors. In the coming year, we hope to reduce the imbalance due to work on the root tree to enable strong scaling to 20,000 cores.

Kernels for both single and double layer charge densities were developed for both multicore CPUs, such as the Intel Nehalem, and GPUs, such as the NVIDIA Tesla 1060C. Our novel *data-aware* queueing system allows the execution of either kernel type without changing the underlying FMM code. We have demonstrated good scalability for $N > 1000$ [14], which will be easily satisfied by our DFT calculations where we expect $N \cong 10^7$.

We have developed a new PETSc compatibility layer for PetFMM that will allow easy integration into the existing DFT code. Input and output data are organized in PETSc **Vec** objects, and **MatShell** wrappers for FMM evaluation allow it to be seamlessly used in all PETSc solvers.

| n_p | r_l | L_v | M | CPU time (sec) | Efficiency |
|-------|-------|-------|-----|----------------|------------|
| 8 | 2 | 4 | 96 | 3.9740e+02 (S) | - |
| 16 | | | | 2.0950e+02 (S) | 95% |
| 32 | | | | 1.1086e+02 (S) | 90% |
| 64 | | | | 5.9088e+01 (D) | 84% |
| 32 | 3 | 5 | 192 | 9.2118e+02 (S) | -, - |
| 64 | | | | 4.8627e+02 (D) | 95%, - |
| 128 | | | | 2.5809e+02 (S) | 89%, 94%* |
| 256 | | | | 1.4380e+02 (D) | 80%, 85%* |
| 512 | | | | 8.6693e+01 (V) | 66%, 70%* |
| 512 | 4 | 6 | 384 | 7.8231e+02 (V) | - |
| 1024 | | | | 5.5052e+02 (D) | 71% |
| 2048 | | | | 4.3421e+02 (D) | 45% |
| 4096 | | | | 3.7705e+02 (V) | 26% |

Figure 3: Strong scaling of PetFMM on CADMOS BG/P. The times reported here represent the total time taken to perform the multipole summation (ParaFMMEvaluate). (S) denotes -mode SMP, (D) denotes -mode DUAL, (V) denotes -mode VN. * indicates efficiency was computed w.r.t the 64 CPU execution time ($p_1 = 64$).

4.2.2 BIBEE Approximation

In preparation for the calculations necessary for dielectric boundary terms in DFT, we have examined approximations for calculation of an electrostatic field in the presence of a dielectric boundary. The BIBEE approximation [15] appears to be an effective option for DT since it relies only on approximating the integral operator in the boundary integral equation (BIE) formulation of electrostatics, rather than specifics of the problem setup and method of evaluation as in the Generalized Born (GB) framework. Moreover, we were able to prove rigorous upper and lower bounds for the BIBEE approximation [16], as opposed to GB.

In recent work, we have deepened the analysis of BIBEE by considering the case of a spherical inclusion [17], for which a complete analytic solution is available. This led to the construction of the superior BIBEE/M approximation and a better understanding of separable approximations for potential solutions with a dielectric jump. We anticipate that this scheme can be directly used in DFT to provide good approximations to the long-range electrostatic potential ϕ . However, it also seems likely that this approximation technique can be leveraged to simplify the calculation of the near-field electrostatic correlations as well.

5 Local Equilibrium Grand Canonical Monte Carlo

This work is in collaboration with Dr. Dezső Boda of the University of Pannonia, Hungary. It stems out of discussions that we had about the dielectric DFT functional on a grant-sponsored trip to his department. This work is not meant to replace any work on DFT, but rather as an alternative method for scientists to use if the DFT is not appropriate for them.

The purpose of the LE-GCMC method is to develop a well-defined molecular model computed by Monte Carlo (MC) simulations coupled to the Nernst-Planck (NP) equation of electrodiffusion:

$$\mathbf{j}^\alpha(\mathbf{r}) = -\frac{1}{kT} D^\alpha(\mathbf{r}) c^\alpha(\mathbf{r}) \nabla \mu^\alpha(\mathbf{r}), \quad (119)$$

where T is temperature, k is Boltzmann's constant, $\mathbf{j}^\alpha(\mathbf{r})$ is the particle flux density ($\alpha = 1, \dots, M$ refers to a diffusing species), $D^\alpha(\mathbf{r})$ is the diffusion coefficient profile, $c^\alpha(\mathbf{r})$ is the density (concentration) profile, $\mu^\alpha(\mathbf{r}) = \mu_0^\alpha(\mathbf{r}) + z^\alpha e \Phi(\mathbf{r})$ is the electrochemical potential profile with $\mu_0^\alpha(\mathbf{r})$ being the chemical potential in the absence of an applied electric field, z^α the valence, e the electronic charge, and $\Phi(\mathbf{r})$ the mean potential. MC is useful for ions at a dielectric interface as well because we have already created a fast method to include dielectrics in the MC and therefore including it in the method outlined below is straight-forward and will constitute one of the next steps of the project.

The LE-GCMC is a big step forward because we suggest (for the first time, to our knowledge) applying MC simulations locally for subvolumes of the simulation cell that are assumed to be in local equilibrium. Because these subvolumes are characterized by their volumes V_i , chemical potentials, μ_i , and the temperature, T , they represent open systems and, therefore, the native ensemble of the simulations in these subvolumes is the GC ensemble. Therefore, we introduce the LE-GCMC method to simulate a globally non-equilibrium steady-state system with spatially varying chemical potential. In this method, we apply independent particle insertion/deletion steps for the various subvolumes with acceptance probabilities

$$p_i^\alpha = \min \left\{ 1, \frac{N_i^\alpha!}{(N_i^\alpha + \chi)!} V_i^\chi \exp \left(-\frac{\Delta U - \chi \mu_i^\alpha}{kT} \right) \right\}, \quad (120)$$

where N_i^α the number of particles of species α in subvolume V_i before insertion/deletion, μ_i^α is the chemical potential of species α in this subvolume, and $\chi = 1$ for insertion, while $\chi = -1$ for deletion (Metropolis sampling). Particle displacements from subvolume V_i to subvolume V_j are accepted with probability

$$p_{i \rightarrow j}^\alpha = \min \left\{ 1, \exp \left(-\frac{\Delta U - (\mu_j^\alpha - \mu_i^\alpha)}{kT} \right) \right\}. \quad (121)$$

The mean electrical potential profile is computed in the simulation “on the fly” by using the inserted ions as test charges. The electrical potentials computed at the position of the inserted ion are averaged over the subvolumes.

ΔU is the energy change associated with the insertion/deletion/movement of an ion and it contains the ion's interaction with an applied potential, $z^\alpha e \Phi^{\text{appl}}(\mathbf{r})$, where $\Phi^{\text{appl}}(\mathbf{r})$ is the solution of Laplace's equation with the prescribed boundary condition. The LE-GCMC steps are coupled only through temperature and energy. The energy change ΔU contains not only the interaction energies between particles in subvolume V_i , but also the effect of particles outside this subvolume. The interactions with these particles can be considered as an external constraint on the particles in subvolume V_i .

The result of the LE-GCMC simulation is a set of density profiles, $\{c^1(\mathbf{r}), \dots, c^M(\mathbf{r})\}$, obtained for a set of chemical potential profiles and the fixed temperature, $\{T, \mu^1(\mathbf{r}), \dots, \mu^M(\mathbf{r})\}$. The LE-GCMC simulation, therefore, provides the same information that DFT does with the difference that it uses the chemical potentials as independent variables of the ensemble instead of the densities. The advantages of the LE-GCMC technique are that (1) it can be applied to three-dimensional systems with a wider variety of geometries and pair-potentials, (2) it provides exact results (apart from statistical and system size errors), while theories necessarily contain approximations, and (3) it provides a mean electrical potential that automatically satisfies Poisson's equation, because Poisson's equation is true in every sampled configuration, and consequently, it is true for their average too. The iteration procedure given in this paper ensures that the resulting mean potential satisfies the prescribed boundary condition.

The LE-GCMC simulation then provides the density profiles for given chemical potential profiles. Substituting these quantities and the diffusion coefficient profiles (it must be provided by the user) into the NP equation, the flux density can be calculated.

There is no guarantee that even an intelligent initial guess for the chemical potential profiles provides flux densities that satisfy the continuity equation. Therefore, we compute new chemical potential profiles that would provide flux densities that satisfy the continuity equation using the density profiles, $c_i^\alpha(n)$, obtained from the LE-GCMC simulation in the n th iteration. These new chemical potential profiles, $\mu_i^\alpha(n+1)$, are used in the LE-GCMC simulations in the next, $(n+1)$ th, iteration. The heart of the iteration algorithm can

be given as follows. The divergence theorem for the i th subvolume is

$$0 = \int_{V_i} \nabla \cdot \mathbf{j}^\alpha(\mathbf{r}) dV = \oint_{S_i} \mathbf{j}^\alpha(\mathbf{r}) \cdot d\mathbf{s}, \quad (122)$$

where S_i denotes the surface of the volume element. If we denote the faces of volume element V_i by S_{ij} on which the densities, chemical potentials, and flux densities are assumed to be constant, the surface integrals can be written as a sum over these faces:

$$0 = \sum_{j, S_{ij} \in S_i} \mathbf{j}^\alpha(S_{ij}) \cdot \mathbf{n}(S_{ij}) a_{ij}, \quad (123)$$

where $\mathbf{n}(S_{ij})$ and a_{ij} denote the outward normal vector and area of face S_{ij} , respectively. Substituting the NP equation for $\mathbf{j}^\alpha(S_{ij})$, we obtain the equation for the computation of the chemical potentials for the next iteration:

$$0 = \sum_{j, S_{ij} \in S_i} D_{ij}^\alpha c_{ij}^\alpha(n) \nabla \mu_{ij}^\alpha(n+1) \cdot \mathbf{n}_{ij} \quad (124)$$

where $D_{ij}^\alpha = D^\alpha(S_{ij})$, $c_{ij}^\alpha = c^\alpha(S_{ij})$, $\mu_{ij}^\alpha = \mu^\alpha(S_{ij})$, and $\mathbf{n}_{ij} = \mathbf{n}(S_{ij})$.

Boundary conditions are that the chemical potential is $\mu^{\alpha,L} = \mu_0^{\alpha,L} + z^\alpha e \Phi^L$ in the left hand side, while it is $\mu^{\alpha,R} = \mu_0^{\alpha,R} + z^\alpha e \Phi^R$ in the right hand side bulk for species α . The bulk chemical potentials, $\mu_0^{\alpha,L}$ and $\mu_0^{\alpha,R}$ corresponding to the prescribed concentrations 0.1 and 1 M were calculated with the Adaptive GCMC method of Malasics and Boda. The electrical potential in the left bath is chosen to be $\Phi^L = 0$, so the value Φ^R gives the voltage.

The calculation domain is divided into slabs indexed from 0 to $N+1$ and centers denoted by x_i . Boundary conditions are set at x_0 and x_{N+1} . The applied potential is a linear function between 0 at x_0 and Φ^R at x_{N+1} in the planar geometry. Chemical potentials and densities in the slabs are denoted by μ_i^α and c_i^α . Quantities on the boundaries of neighboring slabs are denoted by prime. The flux density, the concentration, and the diffusion coefficient on the boundary of the i th and $(i+1)$ th slabs are denoted by $j_i'^\alpha$, $c_i'^\alpha$, and $D_i'^\alpha$, respectively. Eq. 124 can be written for the i th slab as

$$0 = D_i'^\alpha c_i'^\alpha(n) \frac{\mu_{i+1}^\alpha(n+1) - \mu_i^\alpha(n+1)}{x_{i+1} - x_i} - D_{i-1}'^\alpha c_{i-1}'^\alpha(n) \frac{\mu_i^\alpha(n+1) - \mu_{i-1}^\alpha(n+1)}{x_i - x_{i-1}}, \quad (125)$$

where density $c_i'^\alpha$ is obtained from interpolation between c_i^α and c_{i+1}^α . The boundary conditions are $\mu_0^\alpha = \mu^{\alpha,L}$, $\mu_{N+1}^\alpha = \mu^{\alpha,R}$, $c_0^\alpha = c^{\alpha,L}$, and $c_{N+1}^\alpha = c^{\alpha,R}$. This yields N linear equations for the N unknowns, $\{\mu_i^\alpha(n+1), \dots, \mu_i^\alpha(n+1)\}$.

We have done an implementation of the procedure for a one-dimensional test system of ions diffusing through a membrane. This made it possible to make a direct comparison with DFT-PNP results. The results were indistinguishable after just 3 or 4 iterations (not shown). A manuscript of the work was recently published in *Journal of Chemical Theory and Computation*.

Currently work is being done to include dielectric interfaces. This is straight-forward since Dr. Boda's MC simulations already include this feature due to a long-time collaboration to efficiently include it in the simulations. This should prove to be a very useful route for many scientists to include dielectric interfaces into their ion current calculations.

6 Connecting with experiments in nanofluidic devices

Experiments on real-world systems is the ultimate test of any theory and part of this year was designed to interface with experimental systems that could be used to test the real-world applicability of the dielectric

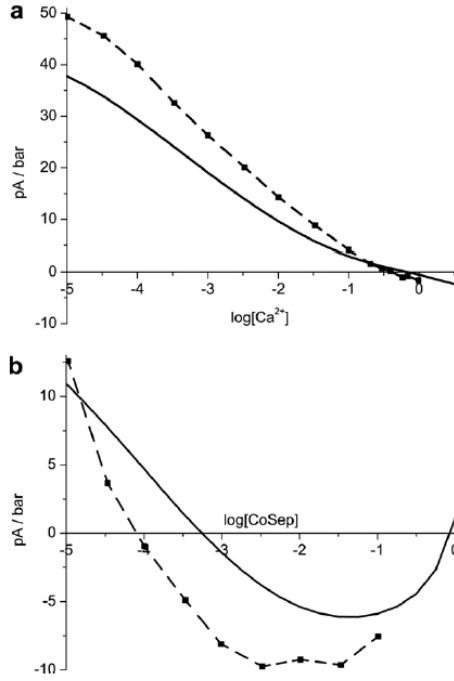


Figure 4: Comparing DFT with charge inversion streaming currents experiments. The solid line is the DFT result and the symbols are the experiments of van der Hayden et al. (PRL, 96:224502). The dashed line connects the symbols and is meant to guide the eye. The change of sign of the current indicates that charge inversion is present. (a) CaCl_2 concentration is increased. (b) CoSepCl_3 concentration is increased.

functional (which is after all the overarching goal of producing such a functional). This work was mainly on nanofluidic devices.

This work is in collaboration with Prof. Sumita Pennathur at the University of California at Santa Barbara. The grant supported trips to UCSB to discuss the work and the one paper that we produced last year with another in preparation.

Fluidic devices can be fabricated with nanometer-scale features using the same techniques used for silicon semiconductors. These devices hold the promise to analyze, separate, concentrate, manipulate, and detect specific molecules with exquisite sensitivity and high throughput. Applications include DNA sequencing, medical testing, and biowarfare defense. These applications can be realized because the fluids are confined to slits or channels whose smallest dimension is tens of nanometers in size (with the other dimensions still macroscopic). The smaller the confining direction is, the more that surface effects—which are negligible in macroscopic systems—come to dominate over normal bulk properties. The ionic current and velocities through these nanoscale electrokinetic devices is then defined by the structure of the electrical double layers at the device walls. Modeling such devices then requires accurate—and hopefully fast-computing—theories to calculate the double layers. DFT is such a theory and that is what we did in a first-of-a-kind application in the field of nanofluidics [18]. In that paper, we examined the effect of finite ion size in nanofluidic devices by modeling the ions as charged, hard spheres. We showed that the ion-ion correlations included in DFT—but absent from Poisson-Boltzmann theory and many of its generalizations—produce a wide range of counterintuitive phenomena (e.g., charge inversion), both in the electrical double layers at device walls and in the resulting qualitatively different pressure-driven and electro-osmotic currents.

We also reproduced very challenging experimental data that involved charge inversion. Also called over-

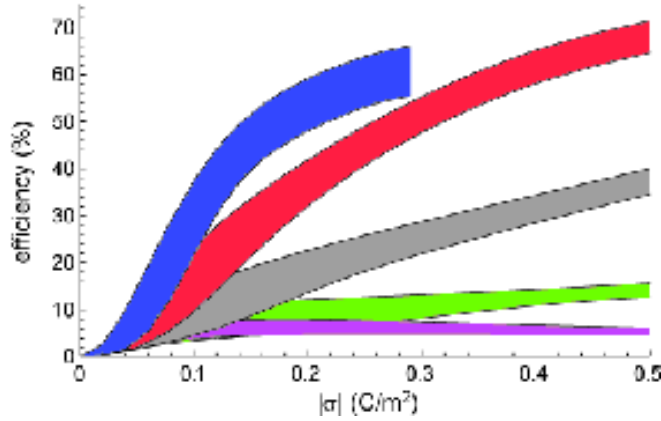


Figure 5: Energy conversion efficiency as a function wall surface charge for ions of diameter (in nm) 0.3 (magenta), 0.6 (green), 0.9 (gray), 1.2 (red), and 1.5 (blue). The surface charge on the slit walls is negative, the slit height is 10 nm, the counterion concentration is 100 mM, its diffusion coefficient is 0.5 m²/s, and the co-ion is Cl⁻. The range of efficiencies for each surface charge is bracketed by choosing the Stern layer height to be 0 or the diameter of the counterion.

charging, charge inversion occurs when more counterions are adsorbed on a charged surface than is necessary to neutralize the surface charge. As a result, a layer of co-ions is adsorbed behind the first layer of counterions. When enough co-ions form this second layer, the mean electrostatic potential can change sign (compared to the potential at the wall surface). Since this potential defines the velocity of the ions when they are driven by an applied voltage, a change of sign indicates a reversal of velocity and this produces qualitatively different results than a potential that does not change sign (as in most of the theories used on nanofluidic devices). DFT is one of the few theories that produces charge inversion and we used it to reproduce—for the first time by any theory that we are aware of—the experiments of Cees Dekker’s lab that showed charge inversion (Fig. 4). This work is also important because it showed that DFT can reproduce experimental data for systems with particles that are trivalent (+3 charge) and large (9 Å in diameter) and at high concentrations (up to 1 M). No other theory like Poisson-Boltzmann we are aware of can do this.

Another nanofluidics application of was recently published in the prestigious *Nano Letters*. This concerned using the ion correlations in DFT to produce very high efficiency in the energy conversion process from pressure to voltage. Ions in nanofluidic devices can be moved either by applying pressure or by applying a voltage. When moved with pressure, the ions produce a streaming potential and this can be used to drive an electrical system. The efficiency of this process was always described as being very low, but this theoretical work did not include the effect of the ions’ size. With DFT we included this and showed that very high efficiencies (>50%) were possible, in principle, and >30% in devices that are fabricated today. This is shown in Fig. 5.

References

- [1] Felipe A. Cruz. Heterogeneous extension of the petfmm a fast multipole library. Presentation at WCCM 2010, Sydney Australia, 2010.
- [2] Felipe A. Cruz, L. A. Barba, and Matthew G. Knepley. PetFMM—a dynamically load-balancing parallel fast multipole library. To appear, *Int. J. Num. Meth. Fluids*; preprint on <http://arxiv.org/abs/0905.2637>; doi:10.1002/nme.2972, 2010.

- [3] George Karypis and V. Kumar. ParMETIS: Parallel graph partitioning and sparse matrix ordering library. Technical Report 97-060, Department of Computer Science, University of Minnesota, 1997. <http://www.cs.umn.edu/metis>.
- [4] George Karypis and Vipin Kumar. A parallel algorithm for multilevel graph partitioning and sparse matrix ordering. *Journal of Parallel and Distributed Computing*, 48:71–85, 1998.
- [5] S. R. McGuffee and A. H. Elcock. Atomistically detailed simulations of concentrated protein solutions: the effects of salt, pH, point mutations, and protein concentration in simulations of 1000-molecule systems. *Journal of the American Chemical Society*, 128:12098–12110, 2006.
- [6] W. T. Rankin. *Efficient parallel implementations of multipole-based N-body algorithms*. PhD thesis, Department of Electrical and Computer Engineering, Duke University, 1999.
- [7] Michael S. Warren and John K. Salmon. A parallel hashed oct-tree N-body algorithm. In *Proceedings of the 1993 ACM/IEEE Conference on Supercomputing*, pages 12–21, New York, 1993. ACM.
- [8] R. Yokota, T. Hamada, J. P. Bardhan, M. G. Knepley, and L. A. Barba. Biomolecular electrostatics simulation by an FMM-based BEM on 512 GPUs. preprint arXiv:1007.4591, July 2010, 2010.
- [9] Knepley, M. G., D. Karpeev, S. Davidovits, R. S. Eisenberg, and D. Gillespie. 2010. An efficient algorithm for classical density functional theory in three dimensions: Ionic solutions. *J. Chem. Phys.* 132:124101.
- [10] Gillespie, D., W. Nonner, and R. S. Eisenberg. 2002. Coupling Poisson-Nernst-Planck and density functional theory to calculate ion flux. *J. Phys.: Condens. Matter* 14:12129-12145.
- [11] Satish Balay, Jed Brown, Kris Buschelman, Victor Eijkhout, William D. Gropp, Dinesh Kaushik, Matthew G. Knepley, Lois Curfman McInnes, Barry F. Smith, and Hong Zhang. PETSc users manual. Technical Report ANL-95/11 - Revision 3.1, Argonne National Laboratory, 2010.
- [12] Dave A. May and Matthew G. Knepley. Optimal, scalable forward models for computing gravity anomalies. *Geophysical Journal International*, 2011. to appear.
- [13] R. Yokota, T. Hamada, J. P. Bardhan, M. G. Knepley, and L. A. Barba. Biomolecular electrostatics simulation by an FMM-based BEM on 512 GPUs. preprint arXiv:1007.4591, July 2010, 2010.
- [14] Felipe A. Cruz. Heterogeneous extension of the petfmm a fast multipole library. Presentation at WCCM 2010, Sydney Australia, 2010.
- [15] J. P. Bardhan. Interpreting the Coulomb-field approximation for Generalized-Born electrostatics using boundary-integral equation theory. *J. Chem. Phys.*, 129 (144105), 2008.
- [16] J. P. Bardhan, M. G. Knepley, and M. Anitescu. Bounding the electro-static free energies associated with linear continuum models of molecular solvation. *J. Chem. Phys.*, 130:104108, 2009.
- [17] Jaydeep P. Bardhan and Matthew G. Knepley. Mathematical analysis of the bibee approximation for molecular solvation: Exact results for spherical inclusions. *Journal of Physical Chemistry*, 2011. to appear.
- [18] Gillespie, D., A. S. Khair, J. P. Bardhan, and S. Pennathur. 2011. Efficiently accounting for ion correlations in electrokinetic nanofluidic devices using density functional theory. *J. Colloid Interface Sci.* 359:520-529.
- [19] Roth, R., D. Gillespie, W. Nonner, and R. E. Eisenberg. 2008. Bubbles, gating, and anesthetics in ion channels. *Biophys. J.* 94:4282-4298.